

Comparison of Inverse and Regular 2-Pyridyl-1,2,3-triazole “Click” Complexes: Structures, Stability, Electrochemical, and Photophysical Properties

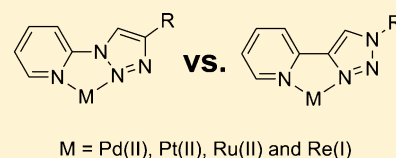
Warrick K. C. Lo,[†] Gregory S. Huff,^{†,§} John R. Cubanski,[†] Aaron D. W. Kennedy,[†] C. John McAdam,[†] David A. McMorran,[†] Keith C. Gordon,^{†,§} and James D. Crowley^{*,†}

[†]Department of Chemistry, University of Otago, P.O. Box 56, Dunedin 9054, New Zealand

[§]MacDiarmid Institute for Advanced Materials and Nanotechnology, Wellington 6140, New Zealand

Supporting Information

ABSTRACT: Two inverse 2-pyridyl-1,2,3-triazole “click” ligands, 2-(4-phenyl-1*H*-1,2,3-triazol-1-yl)pyridine and 2-(4-benzyl-1*H*-1,2,3-triazol-1-yl)pyridine, and their palladium(II), platinum(II), rhenium(I), and ruthenium(II) complexes have been synthesized in good to excellent yields. The properties of these inverse “click” complexes have been compared to the isomeric regular compounds using a variety of techniques. X-ray crystallographic analysis shows that the regular and inverse complexes are structurally very similar. However, the chemical and physical properties of the isomers are quite different. Ligand exchange studies and density functional theory (DFT) calculations indicate that metal complexes of the regular 2-(1-*R*-1*H*-1,2,3-triazol-4-yl)pyridine (*R* = phenyl, benzyl) ligands are more stable than those formed with the inverse 2-(4-*R*-1*H*-1,2,3-triazol-1-yl)pyridine (*R* = phenyl, benzyl) “click” chelators. Additionally, the *bis*-2,2'-bipyridine (bpy) ruthenium(II) complexes of the “click” chelators have been shown to have short excited state lifetimes, which in the inverse triazole case, resulted in ejection of the 2-pyridyl-1,2,3-triazole ligand from the complex. Under identical conditions, the isomeric regular 2-pyridyl-1,2,3-triazole ruthenium(II) bpy complexes are photochemically inert. The absorption spectra of the inverse rhenium(I) and platinum(II) complexes are red-shifted compared to the regular compounds. It is shown that conjugation between the substituent group *R* and triazolyl unit has a negligible effect on the photophysical properties of the complexes. The inverse rhenium(I) complexes have large Stokes shifts, long metal-to-ligand charge transfer (MLCT) excited state lifetimes, and respectable quantum yields which are relatively solvent insensitive.



INTRODUCTION

The copper catalyzed condensation of a substituted azide and a terminal alkyne to form a 1,4-disubstituted 1,2,3-triazole, known as the copper-catalyzed azide–alkyne cycloaddition (CuAAC, Figure 1),¹ has become a widely used tool for creating functionalized ligands for coordination complexes.² While some of these ligands include the 1,2,3-triazole moiety solely as a linking unit, the heterocycle is capable of coordinating to metal centers in a variety of modes (Figure 1).

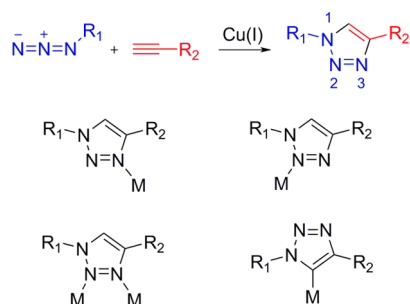


Figure 1. Copper-catalyzed azide–alkyne cycloaddition (CuAAC) reaction (top) and the coordination modes displayed by 1,4-disubstituted 1,2,3-triazole ligands (bottom).

As they are viewed as readily functionalized analogs of the ubiquitous 2,2'-bipyridine (bpy) moiety (**1**, Figure 2), the 2-(1-*R*-1*H*-1,2,3-triazol-4-yl)pyridine family of ligands (**2**, Figure 2) have become an important class of click chelator. These 2-pyridyl-1,2,3-triazole containing ligands have been widely used for the development of coordination complexes^{2b–d} and metallosupramolecular systems³ with interesting catalytic,⁴

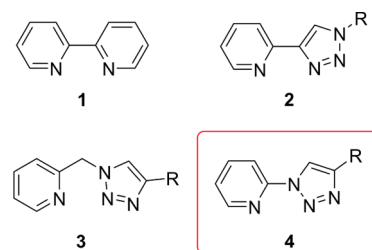


Figure 2. N–N bidentate chelators, 2,2'-bipyridine (**1**), 2-(1-*R*-1*H*-1,2,3-triazol-4-yl)pyridine (**2**, *reg*-pytri), [2-(4-*R*-1*H*-1,2,3-triazol-1-yl)methyl]pyridine (**3**), and 2-(4-*R*-1*H*-1,2,3-triazol-1-yl)pyridine (**4**, *inv*-pytri).

Received: October 24, 2014

electrochemical,⁵ magnetic,⁶ biological,⁷ and photophysical^{5a,7a,b,8} properties. The 2-(1-*R*-1*H*-1,2,3-triazol-4-yl)pyridine (*reg*-pytri, **2**) ligands have been termed regular (*reg*) click chelators as they coordinate through the more electron rich N3 nitrogen atom of the 1,2,3-triazole unit. Inverse (*inv*) 2-pyridyl-1,2,3-triazole click chelators such as **3**, which coordinate through the N2 nitrogen atom, have also been studied.^{6b,9} However, inverse isomers of **2**, the 2-(4-*R*-1*H*-1,2,3-triazol-1-yl)pyridine (*inv*-pytri, **4**) family of chelators, are much less common.¹⁰ This is presumably due to the complications of synthesizing such ligands arising from the ring-chain tautomerism between 2-azidopyridine and pyridotetrazole in solution.^{10b,11} The open chain form is necessary for the CuAAC to proceed, and the conditions required to generate this species from all but the most electron-poor pyridotetrazole units are generally harsh. However, two recent reports have shown that this transformation can now be reliably accomplished under relatively mild conditions.^{11b,12}

Due to our interest in the development of click ligands and complexes we set out to examine the coordination chemistry of the *inv*-pytri family click chelators (**4**). We and others have previously studied the chemistry of *reg*-pytri ligands (**2**) with a range of metal ions, including palladium(II),⁹ⁱ platinum(II),^{9j,13} ruthenium(II),^{5a,8f,g,i,m,n,p,14} and rhenium(I).^{7b,g-j,8c,d,10a,15} In this report we detail the synthesis and properties of the isomeric palladium(II), platinum(II), rhenium(I), and ruthenium(II) *inv*-pytri complexes. The structural, electrochemical, and photophysical properties of these complexes are compared with the known *reg*-pytri analogues. Furthermore, it is shown using competition experiments with the complexes that the *reg*-pytri ligands form more stable complexes than the *inv*-pytri family click chelators. Additionally, it is demonstrated that ruthenium(II) bpy complexes of the inverse click chelators are photochemically active. Irradiation of these complexes with UV light leads to the ejection of the *inv*-pytri ligand from the complex. The isomeric regular *reg*-pytri ruthenium(II) bpy complexes are photochemically inert.

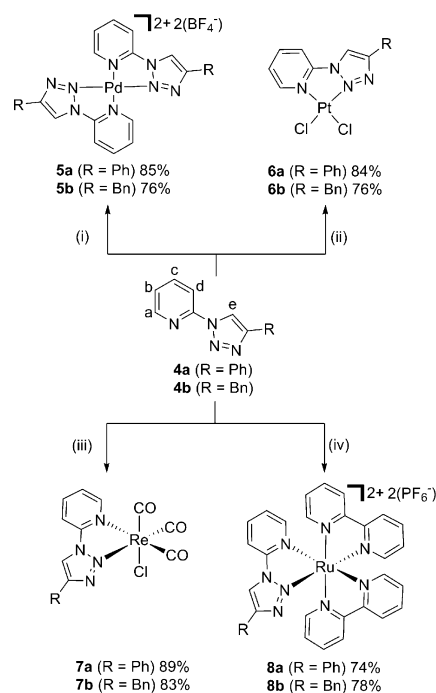
RESULTS AND DISCUSSION

Synthesis and Structures. The *inv*-pytri ligands, 2-(4-phenyl-1*H*-1,2,3-triazol-1-yl)pyridine (**4a**) and 2-(4-benzyl-1*H*-1,2,3-triazol-1-yl)pyridine (**4b**), were synthesized in good yields (63–72%) using modified literature procedures (Supporting Information Scheme S1 and Figures S1–S8).^{11b,12} The palladium(II),⁹ⁱ platinum(II),^{9j,13} ruthenium(II),^{5a,8f,i,m,n,p,14} and rhenium(I)^{7b,g-j,8c,d,10a,15} complexes of the *inv*-pytri ligands (**4a–b**) were synthesized using the methods previously exploited to generate the isomeric *reg*-pytri complexes (Scheme 1). Complexes **5–8** were characterized using elemental analysis, high resolution electrospray ionization mass spectrometry (HRESI-MS), IR, ¹H and ¹³C NMR spectroscopies, and X-ray crystallography (Supporting Information, Figures S9–S47).

The molecular structures of the palladium(II), platinum(II), rhenium(I), and ruthenium(II) complexes of the *inv*-pytri ligands (**4a–b**) were unambiguously confirmed by X-ray crystallography (Figure 3, Tables 1 and 2, and Supporting Information Figures S46–47).

The structures of the palladium(II) and platinum(II) complexes revealed the expected square planar geometry at the d⁸ metal ions. The palladium(II) ions in the complexes (**5a–b**) were coordinated to two *inv*-pytri ligands via the 2-pyridyl nitrogen and the N2 nitrogen atom of the triazole ring (Figure 3a and Supporting Information Figure S46a). The

Scheme 1. Synthesis of Inverse Metal Complexes **5–8**^a



^aConditions: (i) [Pd(CH₃CN)₄](BF₄)₂, CH₃CN, (ii) *cis*-[Pt-(DMSO)₂Cl₂], methanol, reflux, (iii) [Re(CO)₅Cl], methanol, reflux, (iv) (a) *cis*-[Ru(bpy)₂Cl₂], ethanol, microwave (125 °C, 200 W, 1 h), and (iv) (b) NH₄PF₆(aq).

divalent charge of the palladium ions is balanced by two noncoordinating BF₄⁻ anions. The ligands adopted a head-to-tail arrangement around the Pd(II) ions, placing the peripheral substituents as far apart as possible thereby avoiding any unfavorable steric interactions. Additionally, this orientation of the ligands appears to be further stabilized by a hydrogen bonding interaction between the acidic C–H in the 6-position of the pyridyl ring and the N3 nitrogen atom of the 1,2,3-triazole unit on the adjacent ligand, a motif which was also observed for the related regular complexes.⁹ⁱ The molecular structures of platinum(II) complexes (**6a–b**) showed a Pt(II) ion coordinated to an *inv*-pytri ligand and two chloride anions (Figure 3b and Supporting Information Figure S46b).

The molecular structures of the d⁶ rhenium(I) (**7a–b**) and ruthenium(II) (**8a–b**) complexes displayed the expected distorted octahedral coordination environment about the metal ions. The rhenium(I) ions of **7a–b** (Figure 3c and Supporting Information Figure S46c) are coordinated to the bidentate *inv*-pytri ligand, three carbonyl ligands, and a chloride. The carbonyl ligands adopted the expected facial arrangement about the Re(I) cation with a coordinated chloride occupying the other apical position. The ruthenium(II) ions of the inverse **8a–b** complexes are coordinated to two bidentate bpy ligands and one bidentate 2-pyridyl-1,2,3-triazole ligand with divalent charge of the metal ion balanced by two noncoordinating PF₆⁻ anions (Figure 3d and Supporting Information Figure S46d). These tris-bidentate cations are chiral and a racemic mixture of the Λ and Δ enantiomers are present in the crystals.

The M–N_{triazolyl} bond distances and N–M–N angles of the *inv*-pytri chelators (**5–8a–b**) are almost identical to those found in the structures of the analogous *reg*-pytri complexes (Supporting Information Figure S48), and only very subtle

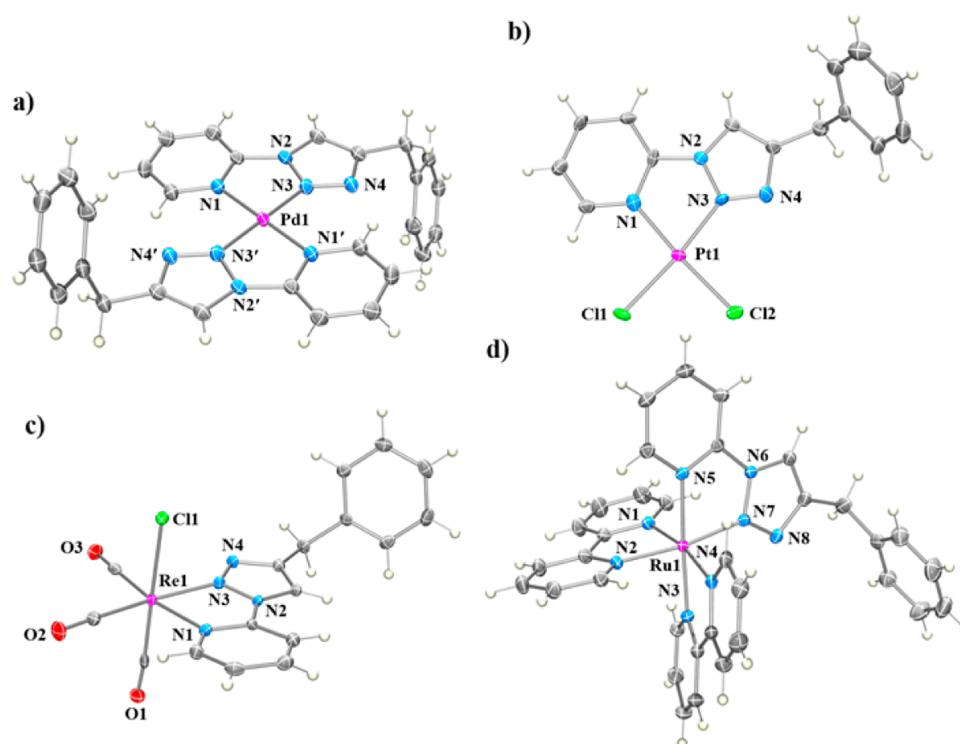


Figure 3. Molecular structures of **5b**·2CH₃CN (a), **6b** (b), **7b**·CH₂Cl₂ (c), and **8b**·2CH₃CN, polymorph 1 (d) are shown as ORTEP¹⁶ diagrams. Counter-anions and solvent molecules were omitted for clarity. The thermal ellipsoids were displayed at the 50% probability level. A figure showing the analogous phenyl complexes (**5**–**8a**) can be found in the Supporting Information (Figure S46).

Table 1. Bond Lengths (Å) for Metal–Pytrri Complexes Crystallized in This Work, Compared to Selected Examples from Literature Reports

complex	<i>inv</i> -pytrri		complex	<i>reg</i> -pytrri	
	M–N _{pyridyl}	M–N _{triazolyl}		M–N _{pyridyl}	M–N _{triazolyl}
5a	2.026(2)	1.989(2)	9a ⁹ⁱ	2.045(2)	2.006(1)
5b	2.026(2)	1.983(2)	9b ⁹ⁱ	2.045(1)	1.995(1)
6a	2.027(3)	1.980(3)	10a ¹³	2.044(7)	1.986(7)
6b	2.01(1)	2.00(1)	10b	<i>b</i>	<i>b</i>
7a	2.24(1)	2.12(1)	11a (NO ₂) ^{8c}	2.214(2)	2.151(2)
7b	2.194(3)	2.148(3)	11a (Cl) ^{8c}	2.205(3)	2.155(3)
8a	2.062(4)	2.050(3)	11b ^{15e}	2.197(5)	2.127(6)
8b (polymorph 1)	2.076(1)	2.037(1)	12a	2.087(9)	2.02(1)
8b (polymorph 2)	2.084(2)	2.022(3)	12b (this work) ^a	2.077(2)	2.063(3)
			12 ^{14c}	2.085(3)	2.038(3)

^aBond lengths from only one of the two [Ru(bpy)₂(*reg*-benzyl)]²⁺ cations in the asymmetric unit were reported. ^bThe molecular structure has not been determined.

differences are observed despite coordination through the potentially more weakly binding N2 nitrogen atom (Tables 1 and 2).

The molecular structures of the complexes show that the *inv*-pytrri (**4a**–**b**) ligands coordinate to metal ions via the more electron deficient N2 nitrogen atom whereas the *reg*-pytrri (**2a**–**b**) ligands coordinate via the more electron rich N3 nitrogen atom. It was postulated that the *inv*-pytrri (**4a**–**b**) ligands would form less stable metal complexes than those of the isomeric *reg*-pytrri (**2a**–**b**) ligands (Figure 4). Ligand exchange experiments and DFT calculations were carried out to examine this (vide infra).

Stability Studies on d⁸ Square Planar Triazole Complexes. A mixture of [Pd(CH₃CN)₄](BF₄)₂ (1 equiv), **4b** (2 equiv), and **2b** (2 equiv) were dissolved in *d*₆-DMSO and

stirred at room temperature for 30 min. The ¹H NMR spectrum (*d*₆-DMSO, 298 K) of the resulting reaction mixture indicated the exclusive formation of the regular palladium complex [Pd(**2b**)₂]²⁺ (**9b**) with *inv*-pytrri ligand **4b** uncomplexed in solution (Scheme 2i and Figure 5). In a second series of competition experiments ligand **2b** (2.1 equiv) and inverse palladium complex **5b** (1 equiv) were dissolved in *d*₆-DMSO and stirred at room temperature for 30 min (Scheme 2ii). Once again, the ¹H NMR spectrum (*d*₆-DMSO, 298 K) of the resulting reaction mixture indicated the exclusive formation of the palladium complex **9b** (Supporting Information Figure S49). These data indicate, as expected, that the *reg*-pytrri ligands (**2**) form more stable coordination complexes than the corresponding *inv*-pytrri systems (**4**). The results from a recent

Table 2. N–M–N Angles (deg) for Metal–Pytri Complexes Crystallized in This Work, Compared to Selected Examples from Literature Reports

complex	<i>inv</i> -pytri		complex	<i>reg</i> -pytri	
	N _{pyridyl} –M–N _{triazolyl}			N _{pyridyl} –M–N _{triazolyl}	
5a	79.11(8)		9a ⁹ⁱ	79.56(6)	
5b	78.99(8)		9b ⁹ⁱ	79.59(5)	
6a	79.8(1)		10a ¹³	79.9(3)	
6b	79.5(4)		10b	<i>b</i>	
7a	74.6(6)		11a (NO ₂) ^{8c}	74.46(8)	
			11a (Cl) ^{8c}	74.6(1)	
7b	73.8(1)		11b ^{15e}	74.4(2)	
8a	77.9(1)		12a	78.8(4)	
8b (polymorph 1)	77.96(6)		12b (this work) ^a	78.3(1)	
8b (polymorph 2)	77.6(1)		12b ^{14c}	78.5(1)	

^aAngles from only one of the two [Ru(bpy)₂(*reg*-benzyl)]²⁺ cations in the asymmetric unit were reported. ^bThe molecular structure has not been determined.

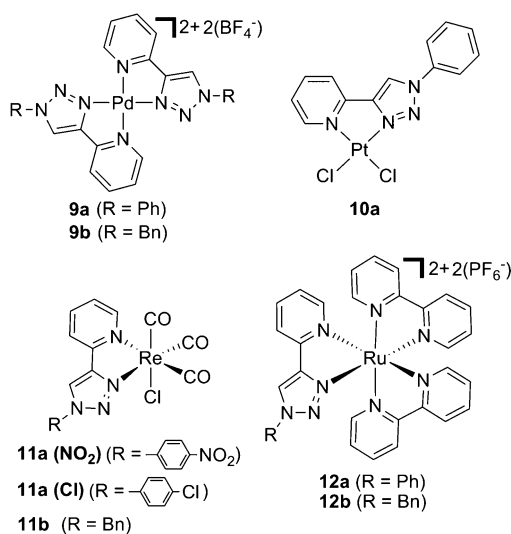


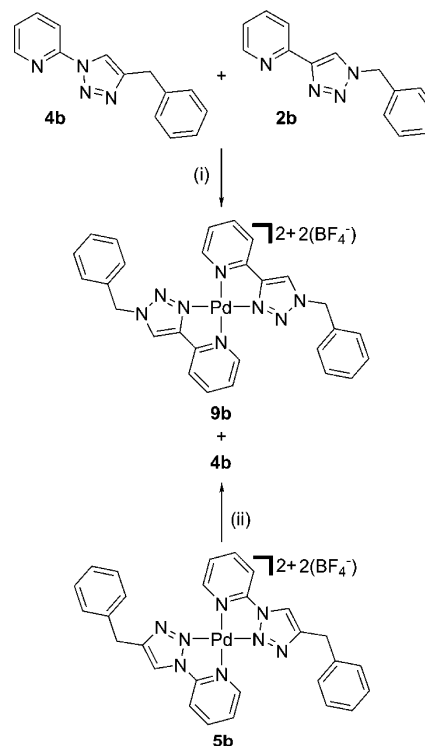
Figure 4. Palladium(II) (9a–b),⁹ⁱ platinum(II) (10a),¹³ rhenium(I) (11a–b),^{8c,15e} and ruthenium(II) 12b^{14c} complexes of *reg*-pytri ligands that have previously been crystallographically characterized. The structures of the ruthenium(II) complexes (12a–b) have been determined as part of this work (Supporting Information Figure S48).

intramolecular competition experiment reported by Sangtrir-utnugul and co-workers are also consistent with our findings.^{10b}

The stability of the palladium complexes was also examined using DFT calculations (B3LYP, Supporting Information Figure S50). Consistent with the experimental results, the DFT calculations indicate that formation of the regular palladium complex 9b by displacement of 4b from 5b is exothermic by 25.7 kcal mol⁻¹. Similarly, formation of 9a by displacement of 4a from 5a is downhill by 23.9 kcal mol⁻¹.

The platinum(II) complexes display similar behavior to the palladium(II) complexes. ¹H NMR spectra of 6b and 10b in *d*₆-DMSO indicate that the [Pt(triazole)Cl₂] complexes decompose to free ligand and [Pt(DMSO)₂Cl₂]. The decomposition of the inverse complex 6b was complete in 2 h whereas the ligand of the corresponding regular complex 10b is not completely decomposed after 4 days (Supporting Information Figures S51–S52).

Scheme 2. Ligand Exchange Experiments^a



^aConditions: (i) [Pd(CH₃CN)₄](BF₄)₂, *d*₆-DMSO, 298 K and (ii) 2b, *d*₆-DMSO, 298 K.

Stability Studies on d⁶ Octahedral Triazole Complexes. The octahedral rhenium(I) (7b and 11b) and ruthenium(II) (8b and 12b) complexes displayed different behavior, compared to the square planar systems, in *d*₆-DMSO (Supporting Information Figures S53–S56). The rhenium(I) inverse complex [Re(4b)(CO)₃Cl] (7b) slowly loses the inverse ligand in *d*₆-DMSO (in the dark). After 4 days approximately 15% of the complex has decomposed.^{10a} Conversely, the regular rhenium(I) complex [Re(2b)(CO)₃Cl] (11b) shows no sign of decomplexation after the same time period. Neither the inverse (8b) nor regular (12b) ruthenium(II) complexes decomposed in *d*₆-DMSO (in the dark) after a week. These data indicate, as expected,^{6b,9f,i,17} that the *reg*-pytri ligands (2) form more stable coordination complexes than the corresponding *inv*-pytri ligands (4), consistent with data obtained from ligand exchange experiments involving the palladium(II) complexes.

Presumably the difference in stability between the inverse and regular ligands is due to the weaker donor ability of the N2 nitrogen atom compared to the N3 nitrogen atom. To examine this further the palladium(II) carbene probe system of Huynh and co-workers¹⁸ was used to obtain an estimate of the ligand donor strength (Supporting Information Scheme S2, Figures S57–S74, and Tables S1–S2). Consistent with the results of the competition experiments the probe system indicated that the *reg*-pytri are stronger donors than the analogous *inv*-pytri compounds (order of donor strength: bpy > phen > *reg*-benzyl 2b > *reg*-phenyl 2a > *inv*-benzyl 4b > *inv*-phenyl 4a).

The different behavior displayed by the d⁸ square planar and d⁶ octahedral complexes is presumably in part due to the different kinetic stability of the metal ions. However, the octahedral Re(I) and Ru(II) complexes, which likely undergo

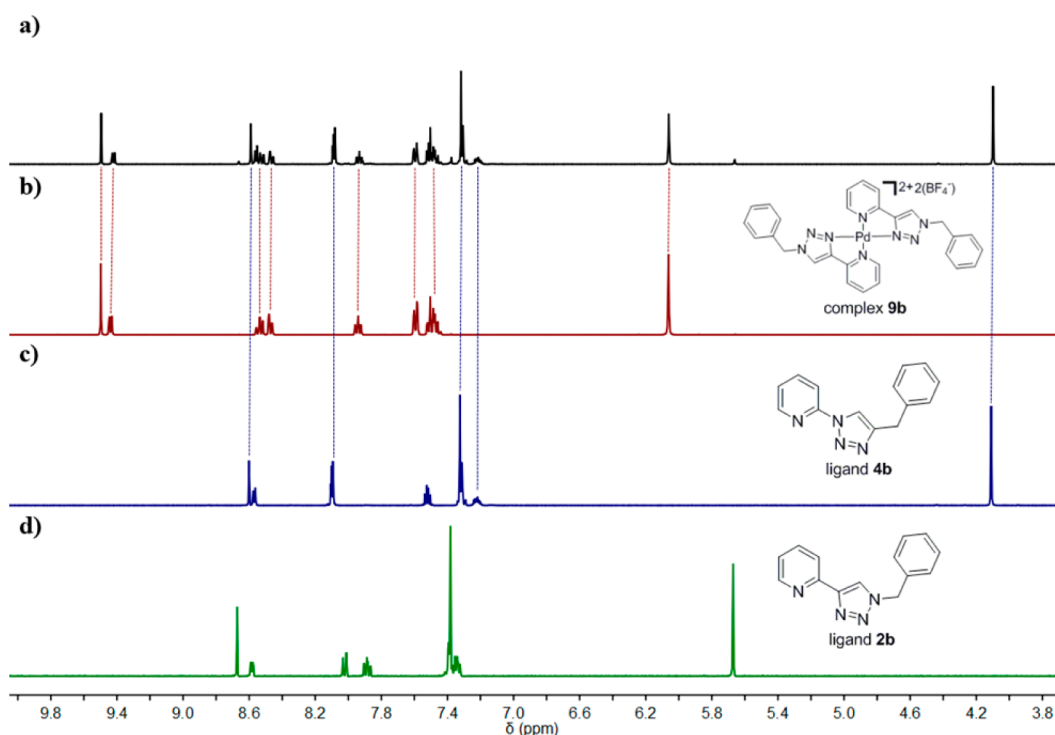


Figure 5. Stacked partial ^1H NMR (400 MHz, d_6 -DMSO, 298 K) spectra of $[\text{Pd}(\text{CH}_3\text{CN})_4](\text{BF}_4)_2$ with 2 equiv each of ligands **2b** and **4b** added (a), complex **9b** (b), ligand **4b** (c), and ligand **2b** (d). The NMR experiment shows that the Pd(II) ion preferentially binds to the regular ligand **2b** over the inverse ligand **4b** to give complex **9b**.

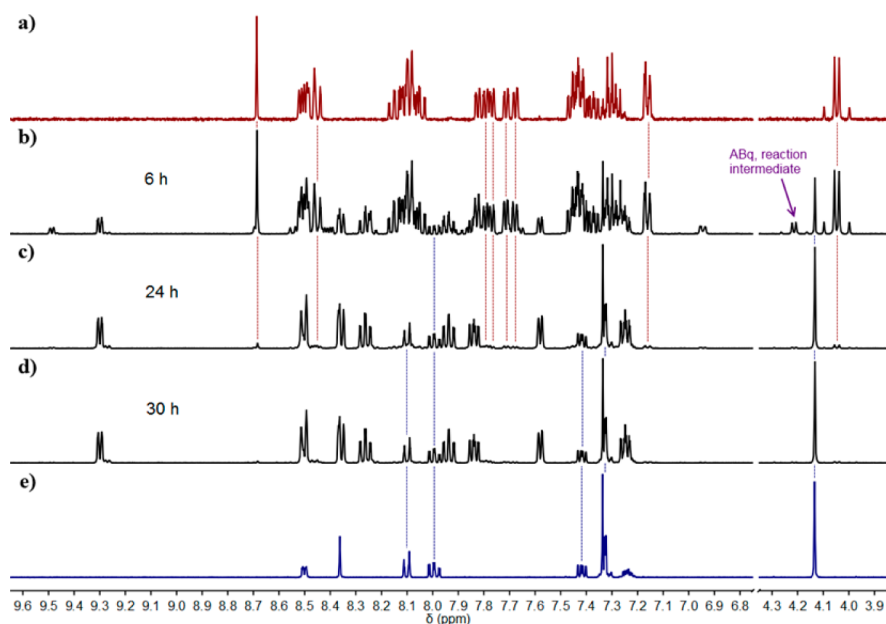
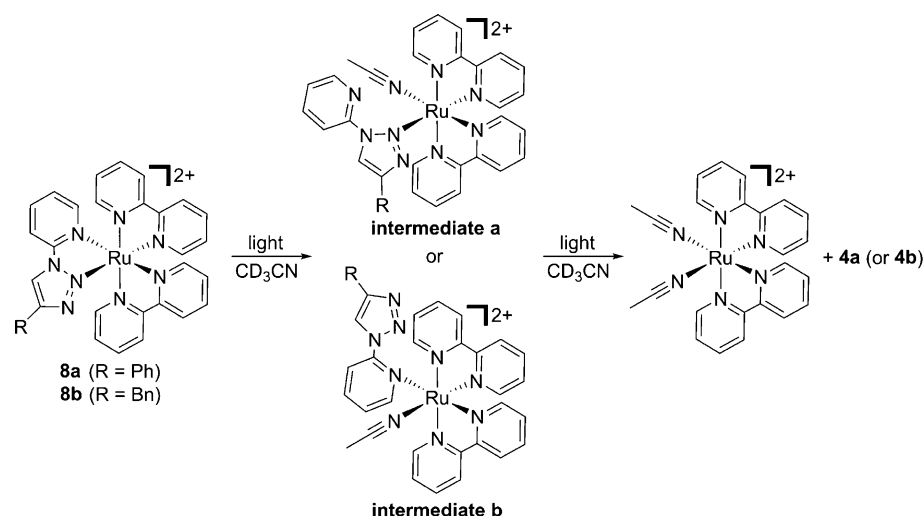


Figure 6. Stacked partial ^1H NMR (400 MHz, CD_3CN , 298 K) spectra of the nonirradiated complex **8b** (a), **8b** after 6 h of irradiation (b), **8b** after 24 h of irradiation (c), **8b** after 30 h of irradiation (d) and the free *inv*-pytri ligand **4b** (e). Expansion shows the benzylic proton signals used for determining the degree of ligand ejection.

the dissociative ligand exchange mechanism, are more long-lived/kinetically stable in d_6 -DMSO, whereas the square planar Pd(II) and Pt(II) complexes, which favor the associative ligand exchange mechanism,¹⁹ decompose far more rapidly in the same solvent.

Photochemical Ligand Exchange. During the course of the stability studies it became apparent that the ligand decomplexation process could be accelerated by light. In the

dark, the inverse rhenium(I) complex **7b** lost 4% of its ligand in d_6 -DMSO after 1 day (Supporting Information Figure S75). When the same complex was irradiated by UV light ($\lambda = 254$ nm), 25% of the ligand was ejected from the complex over the 24 h time period. Interestingly, the regular rhenium(I) complex **11b** shows no sign of ligand ejection after 24 h of irradiation (Supporting Information Figure S76).

Scheme 3. Photochemical Ligand Loss Experiments^a

^aConditions: UV irradiation (254 nm), 35 °C, 24–30 h.

Table 3. Electrochemical Data for Triazole Ligands 2 and 4 and Their Ru(II) bpy Complexes^{a,b}

compound	E_{red3}° (triazole)/V	E_{red2}° (bpy)/V	E_{red1}° (bpy)/V	E_{ox}° (Ru ^{III/II})/V	$E_{\text{ox}}^{\circ} - E_{\text{red1}}^{\circ}$ /mV
2a	-2.31 ^c				
2b	-2.42 ^c				
4a	-2.19 ^c				
4b	-2.28 ^c				
8a	-1.79 (98)	-1.43 (70)	-1.24 (70)	+1.40 (122)	2640
8b	-1.85 (86)	-1.44 (74)	-1.24 (68)	+1.40 (127)	2640
12a	-1.96 (90)	-1.49 (80)	-1.28 (78)	+1.32 (94)	2600
12b	-2.05 (130)	-1.49 (70)	-1.27 (70)	+1.31 (90)	2580
[Ru(bpy) ₃](PF ₆) ₂	-1.68 ^d (66)	-1.42 (58)	-1.24 (56)	+1.29 (86)	2530

^a E° from DPV. ^bPeak-to-peak (mV) separations for the 100 mV s⁻¹ CV experiments. ^cIrreversible reduction, E_{pc} , from 100 mV s⁻¹ CV experiment. ^dThird bpy reduction.

The inverse **8a–b** and regular **12a–b** ruthenium(II) bpy complexes also displayed different photochemical stabilities. Acetonitrile solutions (5 mM) of the inverse complexes **8a–b** were irradiated ($\lambda = 254$ nm) and the reactions monitored using ¹H NMR spectroscopy (Figure 6 and Supporting Information Figure S77). During the course of the irradiation, a series of new peaks, consistent with the free ligand (**4a** or **4b**) and [Ru(bpy)₂(CH₃CN)₂]²⁺, appear in the ¹H NMR spectra of **8a–b**. At the same time the peaks due to the inverse complexes **8a–b** slowly decrease in intensity and then eventually disappear. These data are consistent with the photoactivated ejection of the inverse ligands (**4a** or **4b**) from their corresponding complexes **8a–b**. Similar behavior has recently been documented for related [Ru(diimine)₂(dimethylbpy)]²⁺ and [Ru(diimine)₂(bi-1,2,3-triazole)]²⁺ complexes.²⁰ The rate of ligand ejection in the two complexes is similar. After 24 h the phenyl substituted complex **8a** has ejected 96% of the *inv*-pytri ligand **4a**, whereas the benzyl substituted complex **8b** has liberated 90% of ligand **4b**. This subtle difference in the rate of decomplexation is consistent with the electronic properties of the *inv*-pytri ligands. Acetonitrile solutions of **8a–b** heated, in the absence of light, at 323 K for 15 h show no signs of ligand decomplexation confirming that the process is photochemically but not thermally activated (Supporting Information, Figure S78). Ligand ejection from the complexes **8a–b** is more facile in coordinating solvents. For example, after 24 h of UV irradiation in CD₃CN, 90% of **8b** has ejected the *inv*-pytri

ligand **4b**. After the same time period in *d*₇-DMF and CD₃NO₂ solvents, only 23% and <5% of the ligand **4b**, respectively, had been liberated from **8b**.

Interestingly, under analogous conditions, the isomeric regular ruthenium(II) bpy complexes **12a–b** are photochemically inert. After 24 h of photoirradiation the ¹H NMR spectra (CD₃CN, 298 K) of **12a–b** are essentially unchanged (Supporting Information Figures S79–S80). Only a very small amount (<5%) of the free ligands (**2a–b**) was detected in the reaction mixture.

It is presumed that the decomplexation of the *inv*-pytri ligand from the Ru(II) center proceeds via a two-step process (Scheme 3).^{20a–c} The first step involves the bond dissociation of one of the two Ru–N bonds between the Ru(II) center and the *inv*-pytri ligand and the coordination of an acetonitrile molecule to give a [Ru(bpy)₂(**4a**- or **4b**-κN)(CH₃CN)]²⁺ intermediate. The second step involves the complete dissociation of the *inv*-pytri from the Ru(II) center and the coordination of a second acetonitrile molecule to give a *cis*-[Ru(bpy)₂(CH₃CN)₂]²⁺ and “free” triazole ligand as the final products.

DFT calculations (PBE0,²¹ Supporting Information, Table S3) indicate the intermediate with the triazolyl nitrogen remaining bound (**intermediate a**) has a lower energy than the intermediate with the pyridyl nitrogen bound (**intermediate b**) ($\Delta E = 4.9$ kcal mol⁻¹ for **8b**, 4.5 kcal mol⁻¹ for **8a**). **Intermediate a** then reacts with a second solvent CD₃CN

molecule to form $[\text{Ru}(\text{bpy})_2(\text{CD}_3\text{CN})_2]^{2+}$, and the appropriate free *inv*-pytri ligand (**4a** or **4b**). The ^1H NMR spectrum of an irradiated sample of **8b** displays an AB quartet signal at 4.21 ppm which we propose is due to the presence of an intermediate complex as the signal decreases in intensity upon further irradiation (Figure 6). Previous studies²⁰ have suggested that population of metal-centered triplet (^3MC) states are responsible for the photodissociation behavior observed in these types of complexes. DFT calculation (*vide infra*) suggest that this is also the case for **8a–b**.

Electrochemistry. An electrochemical study of *reg*-pytri (**2a–b**) and *inv*-pytri (**4a–b**) ligands and their Pt(II), Re(I), and Ru(II) complexes (**6–8** and **10–12**) was undertaken using cyclic voltammetry (CV) and differential pulse voltammetry (DPV) in dimethylformamide (DMF) solution. Numerical data are presented in Tables 3 and 4, and representative voltammo-

Table 4. Reduction Potentials of Pt(II) and Re(I) Complexes of Triazole Ligands 2 and 4^a

compound	E_{pc} (triazole)/V	compound	E_{pc} (triazole)/V	E_{pa} ($\text{Re}^{\text{II/I}}$)/V
6a	-1.19 ^b	7a	-1.36 ^b	+1.55 ^b
6b	-1.25 ^b	7b	-1.41 ^b	+1.54 ^b
10a	-1.45 ^b	11a	-1.64 ^b	+1.48 ^b
10b	-1.48 ^b	11b	-1.69 ^b	+1.50 ^b

^aScan rate is 100 mV s⁻¹ for CV experiments. ^bIrreversible process; E_{pc} or E_{pa} is given instead of E° .

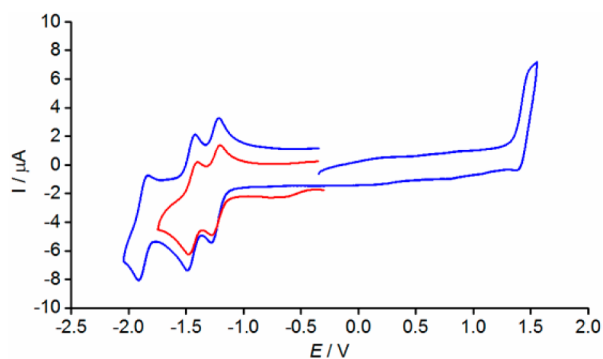


Figure 7. Cyclic voltammograms of **8b** (1 mM) in DMF. The blue trace shows all four electrochemical processes (potential window = -2.0 to +1.6 V) while the red trace shows only the two bpy-based reductions (potential window = -1.7 to -0.3 V): supporting electrolyte 0.10 M Bu_4NPF_6 , scan rate 100 mV s⁻¹, potential vs decamethylferrocene reference $[\text{Fc}^*]^{+/0} = 0.00$ V.

grams illustrated in Figure 7 and the Supporting Information (Figures S81–S82). For the ruthenium(II) complexes (**8a–b** and **12a–b**) the electrochemical cell was wrapped to exclude light and minimize the possibility of photocatalyzed ligand substitution reactions.

The electrochemistry in DMF of the uncoordinated *reg*-pytri (**2a–b**) and *inv*-pytri (**4a–b**) ligands features an irreversible reduction below -2 V (vs $[\text{Fc}^*]^{+/0}$, Table 3). The effect of phenyl and benzyl substituents on the observed reduction is, as predicted, the electron-withdrawing phenyl appended ligands being ca. 100 mV easier to reduce than their benzyl analogues. Additionally, the *inv*-pytri ligands are >100 mV easier to reduce than their *reg*-pytri counterparts. The combination of these effects gives a series in the order of E_{pc} (increasingly negative

potential required): *reg*-benzyl **2b** > *reg*-phenyl **2a** > *inv*-benzyl **4b** > *inv*-phenyl **4a**.

The electrochemistry of regular ruthenium(II) complex **12b** and the archetypal $[\text{Ru}(\text{bpy})_3]^{2+}$ in acetonitrile has been reported.^{5a,14c} Their behavior in DMF follows the same pattern and is similarly exhibited by the new ruthenium(II) complexes **8a–b** and **12a** (Figure 7). Thus, sweeping to cathodic potential gives rise to two reversible reductions associated with the bpy ligands, and a quasi-reversible reduction of the 2-pyridyl-1,2,3-triazole ligand. Anodic scans show the expected $\text{Ru}^{\text{III/II}}$ oxidation couple. Substitution of one of the bpy ligands on $[\text{Ru}(\text{bpy})_3]^{2+}$ with an inverse triazole ligand has no effect (within the experimental error, ± 20 mV) on the reduction potential of the remaining two bpy ligands (Table 3). The effect of a regular triazole ligand is a small cathodic shift of 40 mV and 70 mV for E_{red1}° and E_{red2}° , respectively. The effect on the ruthenium oxidation potential is the reverse, with a small anodic shift (20–30 mV) for the *reg*-pytri complexes; for *inv*-pytri complexes **8a–b** the shift is 110 mV. Both effects are consistent with the inverse triazole ligands having poorer electron donating ability than the regular counterparts. For **8a–b** and **12a–b**, scanning to an increasingly cathodic potential results in the observation of a third reduction which is associated with the 2-pyridyl-1,2,3-triazole group. Compared to the uncoordinated ligands, bidentate coordination to ruthenium imparts stability; the reductions are observed as a quasi-reversible couple, and are shifted ca. 400 mV in the positive direction consistent with the lowering of electron density on the triazole group. The order of reduction potentials (E_{red3}°) with respect to regular/inverse and phenyl/benzyl substitution is as per E_{pc} of the uncoordinated ligands.

The electrochemistry of rhenium(I) complexes **11a–b** of *reg*-pytri ligands in dichloromethane (CH_2Cl_2) solution has previously been described.^{8d} Similar redox behavior is observed for these compounds in DMF solution. The results and those for the *inv*-pytri complexes **7a–b** are given in Table 4, and a representative voltammogram, that of **7b**, is given in the Supporting Information (Figure S81). An irreversible oxidation associated with the $\text{Re}^{\text{II/I}}$ couple occurs near the solvent limit. For complexes **7a–b** there is a small anodic shift (ca. 50 mV) of $E_{\text{pa}}(\text{Re}^{\text{II/I}})$ with respect to the *reg*-pytri analogues **11a–b**, the same effect has been seen for the ruthenium(II) systems, and again is consistent with the poorer electron donating ability of the *inv*-pytri ligands. An irreversible ligand reduction is observed in the range from -1.3 to -1.7 V. The order of reduction potentials (E_{pc}) with respect to regular/inverse and phenyl/benzyl substitution pattern follows that of the uncoordinated ligands and ruthenium(II) compounds as described above.

The electrochemical behavior of *reg*-pytri platinum(II) complexes **10a–b** in DMF (Table 4) resembles that described in CH_2Cl_2 solutions.¹³ Coordination to the metal shifts the irreversible ligand-based reduction (Supporting Information Figure S82) in the predicted anodic direction, as described above for the ruthenium(II) and rhenium(I) systems. Again there is a small variation in shifting between phenyl and benzyl triazole substituents, and for the complexes (**6a–b**) of the *inv*-pytri ligands reduction is shifted ca. 250 mV anodically of the regular variant.

Photophysical Characterization. The electronic absorption and photophysical properties of the complexes were examined to further understand the differences between the regular and inverse pytri ligands. The absorption spectra of the

inverse and regular complexes showed marked differences (Figure 8 and Supporting Information Figures S83–84). The origin of these differences was examined in more detail for the Pt(II), Re(I), and Ru(II) triazole complexes (vide infra).

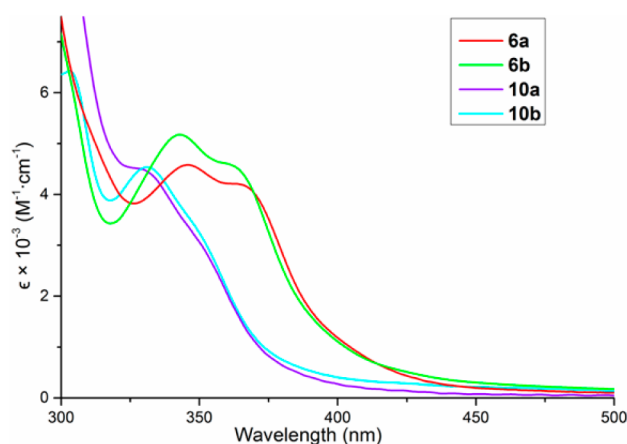


Figure 8. Electronic absorption spectra of the dichloroplatinum(II) complexes (**6a–b** and **10a–b**) in DMF.

Photophysical Properties of the Platinum Complexes.

The electronic absorption spectra of the *inv*-pytri (**6a–b**) and *reg*-pytri (**10a–b**) platinum(II) complexes are shown in Figure 8. The lowest energy absorption for all complexes has an extinction coefficient consistent with a metal-to-ligand charge transfer (MLCT) band. This band is significantly red-shifted for the inverse complexes compared with the regular complexes and the substituent group has very little effect. The MLCT band appears to be split into two partially resolved bands. This is a feature commonly seen in Pt(II) complexes that has been attributed to vibronic coupling in some cases²² and the presence of two separate electronic transitions in others.²³ Resonance Raman spectroscopy was used to study the absorption properties further (Supporting Information Figures S85–S86).

Resonance Raman experiments at 351, 356, and 364 nm probed the split MLCT band of the Pt(II) complexes **6a–b**. The enhancement pattern is similar to that seen in the rhenium complexes (vide infra). The same bands are enhanced at all three wavelengths, implying that this is a single MLCT band split by vibronic coupling. No enhancement of the phenyl breathing mode is seen in **6a** showing that the substituents have little involvement in the MLCT transitions (vide infra). Resonance Raman experiments at 407 and 413 nm were used to probe the tail of the MLCT band. Here an unusual enhancement pattern is found where only four of the 11 bands enhanced at 351–364 nm for **6a** appear. This could be explained by resonant de-enhancement of some vibrational modes due to forbidden d–d transitions.²⁴

The platinum complexes were not found to be emissive in DMF solution at room temperature. It is rare for dichloroplatinum(II) complexes to be emissive²⁵ due to low-lying d–d transitions.²²

Photophysical Properties of the Rhenium Complexes.

Electronic absorption and emission spectra for rhenium(I) complexes **7a** and **7b** in CH₂Cl₂ solution are shown in Figure 9. The absorption maxima of **7a–b** are red-shifted compared to the regular “click” complexes reported previously.^{8d} The phenyl substituent causes a slight red-shift when compared to the

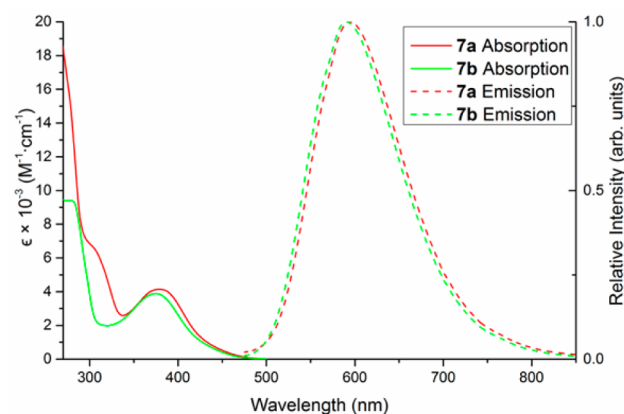


Figure 9. Electronic absorption and emission spectra for the rhenium(I) complexes **7a** and **7b** in CH₂Cl₂ at 298 K.

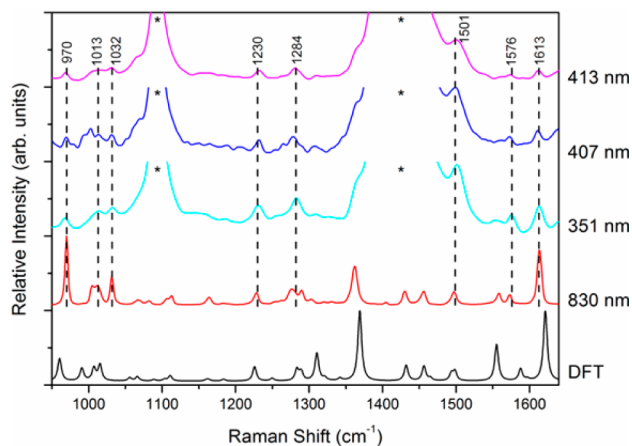
corresponding benzyl substituted complex **7b** and the appearance of a shoulder at 307 nm. The red-shifted absorption is consistent with the electrochemical results discussed above. Time dependent density functional theory (TD-DFT) calculations were used to model the electronic absorption spectra. The results are summarized in Table 5 along with electron transition densities calculated with GaussSum.²⁶ Relevant frontier orbitals are shown in the Supporting Information (Figure S87). The lowest energy band of both compounds is composed of two MLCT transitions. The lower of the two (MLCT – 1) is found in the tail of the band and is mostly due to the highest occupied molecular orbital (HOMO) to lowest unoccupied molecular orbital (LUMO) transition. The second lowest transition (MLCT – 2) is predominantly the HOMO – 1 to LUMO transition and has a much stronger oscillator strength. The donor orbitals are mostly localized on the metal center for **7b**, however, for **7a** the MLCT transitions have a very small contribution from the phenyl ring. Although the phenyl substituent in **7a** has an insignificant effect on the energy of the MLCT transitions, conjugation between the triazolyl and phenyl rings appears to be responsible for the 307 nm shoulder which **7b** lacks. This transition is essentially an intraligand charge transfer (ILCT) from the phenyl and triazolyl rings to the pyridyl ring. Further ILCT and MLCT transitions are expected at higher energy.

Raman spectroscopy was used to better understand the electronic structure of rhenium(I) complexes **7a** and **7b** (Figure 10 and Supporting Information Figure S88). Nonresonant spectra at 830 nm excitation were compared to spectra simulated by DFT calculations with B3LYP. The most significant difference between **7a** and **7b** is the very strong band at 1613 cm⁻¹ in the spectrum of **7a**. The 1613 cm⁻¹ band is composed of pyridyl and phenyl breathing modes, predicted to be within 0.6 cm⁻¹ of each other by the DFT calculations. The intensity of these modes is known to be sensitive to the degree of conjugation and the twist angle between aromatic rings.²⁷ The pyridine band shifts to 1616 cm⁻¹ for the benzyl complex and the aryl mode appears as a shoulder at 1604 cm⁻¹. These bands are much weaker than those in **7a** due to the lack of conjugation between the triazole and benzyl rings.

Resonance Raman spectroscopy was used to probe the MLCT transitions of the Re(I) complexes **7a–b**. The enhancement pattern is nearly identical at all wavelengths and the same pattern is seen for both complexes. Several triazole and pyridine based modes are enhanced. It was not possible to

Table 5. Summary of the Relevant Experimental and Simulated Electronic Transitions for the Inverse Rhenium Complexes (7a–b)

		λ_{exp}	ϵ ($\text{M}^{-1} \text{cm}^{-1}$)	λ_{calc}	f	orbital contributions (%)	electron transition density difference (%)			
							Re(CO) ₃ Cl	pyridine	triazole	R
7a	MLCT – 1	379	4140	405	0.0040	H → L (68), H – 1 → L (18)	86 → 9	1 → 51	8 → 39	6 → 1
	MLCT – 2	379	4140	381	0.0880	H – 1 → L (68), H → L (17)	91 → 9	3 → 51	3 → 39	2 → 1
	ILCT	305 (sh)	6580	321	0.0589	H – 3 → L (69)	20 → 9	3 → 51	22 → 39	56 → 1
	MLCT – 3	276 (sh)	16000	312	0.0178	H – 2 → L (70)	85 → 2	1 → 87	8 → 9	6 → 2
7b	MLCT – 1	374	3840	402	0.0062	H → L (97), H – 1 → L (2)	94 → 9	1 → 52	4 → 39	1 → 0
	MLCT – 2	374	3840	379	0.0886	H – 1 → L (96), H → L (2)	94 → 9	3 → 52	3 → 39	0 → 0
	MLCT – 3	281	9380	311	0.0161	H → L + 1 (98)	94 → 2	1 → 88	4 → 10	1 → 0

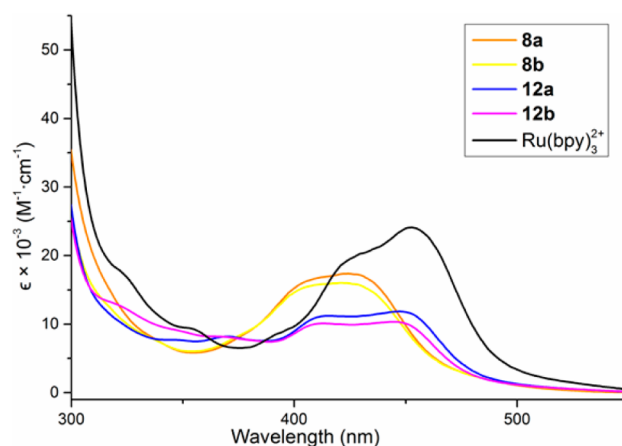
**Figure 10.** Raman spectra of the rhenium complex 7a (3 mM, in DMF) at 298 K. Solvent bands are indicated by an asterisk (*).

differentiate between the two MLCT bands predicted by TD-DFT because each involves the same acceptor orbital, and therefore, produce the same enhancement pattern. The signal corresponding to the phenyl/pyridyl breathing mode discussed above is only slightly enhanced in the resonance Raman spectra for 7a, further showing that the substituent is not involved in the MLCT transitions.

The photophysical properties of the inverse (7a–b) and regular (11a–b) rhenium(I) complexes were studied and compared. A broad structureless emission band typical for this class of complex is seen with 351 nm excitation (Figure 9). The emission spectra of the inverse complexes are red-shifted compared to that of the regular complexes. Emission quantum yields and lifetimes were measured in both CH₂Cl₂ and CH₃CN (Table 6). All of the triazole complexes have improved lifetimes and quantum yields compared to the prototypical 1,10-phenanthroline²⁸ and bpy²⁹ complexes in CH₂Cl₂. The

quantum yields for the inverse complexes in both solvents are comparable to alkyl-substituted inverse 2-pyridyl-1,2,3-triazole rhenium(I) complexes measured in DMSO/water mixtures recently reported by Polcar and co-workers.^{10a} The regular Re(I) complexes (11a–b) appear to be more sensitive to coordinating solvents as shown by significantly longer lifetimes and quantum yields in CH₂Cl₂ compared to CH₃CN. The radiative (k_r) and nonradiative (k_{nr}) decay rate constants were calculated from the quantum yields and lifetimes. Nonradiative decay is faster for the higher energy emitting regular complexes which is counter to what is expected from the energy gap law.²⁹

Photophysical Properties of the Ruthenium Complexes. The electronic absorption spectra of the ruthenium(II) 2-pyridyl-1,2,3-triazole complexes (8a–b and 12a–b) are shown in Figure 11 with that of [Ru(bpy)₃]²⁺ for comparison.

**Figure 11.** Electronic absorption spectra for the ruthenium(II) complexes (8a–b, 12a–b, and [Ru(bpy)₃]²⁺) in CH₂Cl₂ at 298 K.

The MLCT band for the Ru(II) 2-pyridyl-1,2,3-triazole complexes is blue-shifted compared to [Ru(bpy)₃]²⁺, and the

Table 6. Photophysical Properties of the Rhenium(I) Complexes (7a–b and 11a–b) in Argon Saturated Solutions at 298 K

solvent	complex	λ_{Abs} (nm)	λ_{Em} (nm)	τ (μs) ^a	Φ ^a	$k_r \times 10^4$ (s^{-1})	$k_{nr} \times 10^5$ (s^{-1})
CH ₂ Cl ₂	7a	379	596	1.3	0.053	4.1	7.7
	7b	374	591	1.3	0.053	4.1	7.7
	11a	337	550	0.88	0.087	10	11
	11b	346	547	0.80	0.049	6.1	12
CH ₃ CN	7a	359	593	0.83	0.057	6.9	12
	7b	356	589	1.1	0.049	4.5	9
	11a	336	532	0.16	0.036	23	62
	11b	330	532	0.10	0.012	12	100

^a ±10%.

extinction coefficients are reduced by about one-third. This implies that the acceptor orbitals for the MLCT transitions remain bpy^* based. Therefore, the blue-shift is likely a result of a decrease in the $d\pi$ donor orbital energy level. Presumably this is because the triazole is a better π -acceptor than the pyridine which it replaces.^{5a,8n,30} This is consistent with the electrochemical data which show that the triazole complexes have a higher oxidation potential compared to $[\text{Ru}(\text{bpy})_3]^{2+}$ but a mostly unchanged first reduction potential. A plot of the MLCT excitation energy vs the E_{ox} shows a linear relationship as has been seen in other Ru(II) complexes (Supporting Information Figure S89).³¹

Further evidence for a bpy-based acceptor orbital was obtained from resonance Raman spectra (Figure 12). The

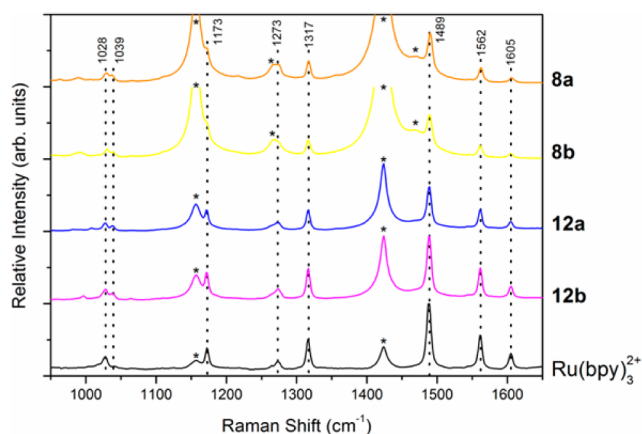


Figure 12. Resonance Raman spectra (458 nm excitation) of the ruthenium(II) complexes (**8a–b**, **12a–b**, and $[\text{Ru}(\text{bpy})_3]^{2+}$) at 1 mM in CH_2Cl_2 . Solvent bands are indicated by an asterisk (*).

458 nm excitation wavelength was used to probe the lowest energy band of all ruthenium complexes. The Ru(II) 2-pyridyl-1,2,3-triazole complexes show enhancement of bands at 1028, 1039, 1273, 1317, 1489, 1562, and 1605 cm^{-1} which is indicative of an $\text{Ru} \rightarrow \text{bpy}$ MLCT transition.³² These are the same modes enhanced for $[\text{Ru}(\text{bpy})_3]^{2+}$, showing that the triazolyl moiety is not involved in the lowest energy MLCT transition.

The regular Ru(II) triazole complexes (**12a–b**) were found to be very weakly emissive in CH_2Cl_2 at 298 K (quantum yield = 0.001)⁸ⁿ while no emission was observed for the inverse Ru(II) complexes (**8a–b**) (Supporting Information Figure S90). Excited state lifetimes for all the ruthenium(II) complexes were shorter than the time resolution of our instrument (<10 ns). Despite the fact that these complexes possess an $^3\text{MLCT}$ state with the excited electron localized on one of the bpy ligands this state is very short-lived in fluid solution due to rapid relaxation to the ground state. This is likely mediated by a low-lying nonemissive ^3MC state as has been seen in similar complexes.³³ DFT calculations were used to further understand this behavior.

The ^3MC states are characterized by population of antibonding d orbitals. The result is elongation of the metal–ligand bonds along the orbital axis, rapid relaxation to the singlet ground state, and potentially ligand loss. Using a method developed by Persson and co-workers,³⁴ ground state, $^3\text{MLCT}$, and ^3MC states were optimized for all the ruthenium complexes. The structural parameters and relative energies are given in the Supporting Information (Table S4). The

geometries of the ground state and $^3\text{MLCT}$ states are very similar to all Ru–N bonds calculated to be about 2.1 Å. Two ^3MC states were optimized for each triazole complex with elongation of the Ru–N bonds along the a or b axes as defined in Figure 13. These correspond to the $\text{Ru}-\text{N}_{\text{triazolyl}}$ or $\text{Ru}-$

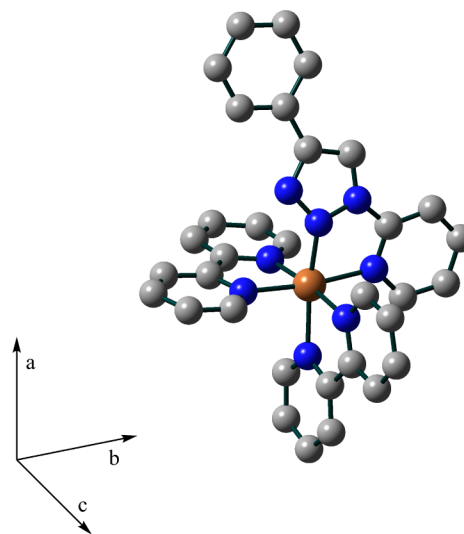


Figure 13. $^3\text{MLCT}$ state of **8a** and axes used for comparing the triplet state geometries.

$\text{N}_{\text{pyridyl}}$ bonds and the Ru–N bond of the bpy ligand *trans* to it. These are referred to as the $^3\text{MC}_{\text{tri}}$ and $^3\text{MC}_{\text{pyr}}$ states, respectively. In the $^3\text{MC}_{\text{tri}}$ state the $\text{Ru}-\text{N}_{\text{triazolyl}}$ bond length is increased to about 2.5 Å while the *trans*- $\text{Ru}-\text{N}_{\text{bpy}}$ bond increases to about 2.3 Å. Elongation along the *b* axis in the $^3\text{MC}_{\text{pyr}}$ state is more pronounced with a $\text{Ru}-\text{N}_{\text{pyridyl}}$ bond length of about 2.6 Å and a *trans*- $\text{Ru}-\text{N}_{\text{bpy}}$ bond of about 2.4 Å. One ^3MC state with elongation of a pair of *trans*-Ru–N bonds in $[\text{Ru}(\text{bpy})_3]^{2+}$ was optimized for comparison. The bond lengths increase from about 2.1 Å in the ground and $^3\text{MLCT}$ state to 2.45 Å in the ^3MC state.

The relative energies of the triplet states play a factor in controlling the rate of decay of the excited state. All relaxed ^3MC states were calculated to be more stable than their corresponding $^3\text{MLCT}$ states. The driving force for decay from the $^3\text{MLCT}$ to ^3MC state ($\Delta E_3 = E_{\text{MC}} - E_{\text{MLCT}}$) was found to be larger for most $^3\text{MC}_{\text{tri}}$ and $^3\text{MC}_{\text{pyr}}$ states compared to the ^3MC state of $[\text{Ru}(\text{bpy})_3]^{2+}$ (Figure 14 and Supporting Information Table S4). This is likely to be responsible for the lack of phosphorescence from the $^3\text{MLCT}$ states.³⁵ All ^3MC states are lower in energy than their corresponding $^3\text{MLCT}$ states. The energy gap between these states ($\Delta E_3 = E_{\text{MC}} - E_{\text{MLCT}}$) is comparable for all complexes. This agrees with previous reports that the shape of the triplet potential energy surface plays more of a role in determining the stability of the emissive state than ΔE_3 does.³⁵

In three out of four Ru(II) triazole complexes, elongation of the $\text{Ru}-\text{N}_{\text{pyridyl}}$ bond was more favorable than elongation of the $\text{Ru}-\text{N}_{\text{triazolyl}}$ bond suggesting that the $\text{Ru}-\text{N}_{\text{pyridyl}}$ bond is more labile, and therefore, more likely to break in photochemical substitution when the ^3MC state is populated. This is consistent with the results from DFT calculations discussed earlier that reaction **intermediate a** (triazolyl N bound) has a lower energy than **intermediate b** (pyridyl N bound) in Scheme 3.

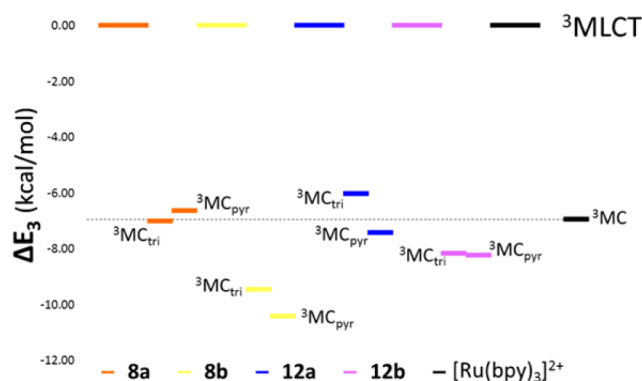


Figure 14. Energy level diagram of the ruthenium(II) complexes triplet state energies. ΔE_3 is the energy difference between the ${}^3\text{MC}$ and ${}^3\text{MLCT}$ states.

CONCLUSION

Using the “click” method developed by Wang, Hu, and co-workers¹² we have been able to readily synthesize two *inv*-pytri click ligands, 2-(4-phenyl-1*H*-1,2,3-triazol-1-yl)pyridine and 2-(4-benzyl-1*H*-1,2,3-triazol-1-yl)pyridine in good yield. The palladium(II), platinum(II), rhenium(I), and ruthenium(II) complexes of these *inv*-pytri ligands were synthesized and characterized by elemental analysis, HRESI-MS, IR, ${}^1\text{H}$, and ${}^{13}\text{C}$ NMR spectroscopies, and in each case the molecular structures confirmed by X-ray crystallography. The properties of these *inv*-pytri complexes have been compared to the isomeric regular compounds. Structurally the regular and inverse complexes are very similar, only very subtle differences in the bond lengths and angles of the complexes were observed. However, the chemical and physical properties of the isomers are quite different. Ligand exchange studies and DFT calculations indicate that metal complexes of the *reg*-pytri ligands are more stable than those formed with the *inv*-pytri click chelators. Additionally, it is shown that ruthenium(II) bpy complexes of the inverse click chelators are photochemically active, photoirradiation of these compounds leads to the ejection of the *inv*-pytri ligand from the complex. Under identical conditions the isomeric *reg*-pytri ruthenium(II) bpy complexes are photochemically inert. DFT calculations show that ligand ejection from the *inv*-pytri complexes is likely the result of populating the low-lying metal-centered triplet states.

The electronic properties of the complexes of these *inv*-pytri ligands have been examined using UV–vis, Raman and emission spectroscopies, cyclic voltammetry, and DFT calculations and were shown to be markedly different from the corresponding *reg*-pytri complexes. The absorption spectra of the inverse rhenium(I) and platinum(II) are red-shifted relative to the regular analogues, and this suggests that new derivatives of these inverse compound could be used to develop new optically interesting materials.³⁶ In particular the rhenium(I) tricarbonyl complexes of the inverse ligands have long excited state lifetimes and high quantum yields which is promising for their use as phosphorescent bioprobes.^{10a} Additionally, the photoactivated ligand ejection behavior of the *inv*-pytri ruthenium(II) bpy complexes could be exploited to develop new photoactivated anticancer agents.^{20d–g} Efforts to use these *inv*-pytri ligands in these and other areas are underway.

EXPERIMENTAL SECTION

General Methods. All reagents were laboratory reagent grade or better and used as received. The ligands **2a** and **2b**⁹ⁱ and complexes $[\text{Pd}(\mathbf{2a})_2](\text{BF}_4)_2$ (**9a**),⁹ⁱ $[\text{Pd}(\mathbf{2b})_2](\text{BF}_4)_2$ (**9b**),⁹ⁱ *fac*- $[\text{Re}(\mathbf{2a})-(\text{CO})_3\text{Cl}]$ (**11a**),^{8d} and *fac*- $[\text{Re}(\mathbf{2b})(\text{CO})_3\text{Cl}]$ (**11b**)^{8d} were prepared using our previously reported methods. Platinum(II) precursor *cis*- $[\text{Pt}(\text{DMSO})_2\text{Cl}_2]$ was prepared by a literature method.³⁷ A CEM S-class microwave reactor was used to carry out microwave enhanced reactions. All NMR spectra were recorded at 298 K. One-dimensional (${}^1\text{H}$ and ${}^{13}\text{C}$) and two-dimensional (gCOSY, TOCSY, HSQCAD, and gHMBCAD) NMR spectra were recorded either on a Varian/Agilent 400-MR or Varian/Agilent 500 MHz AR spectrometer. All chemical shifts (δ) are reported in parts per million (ppm). ${}^1\text{H}$ NMR chemical shifts are referenced to residual solvent peaks (CHCl_3 : ${}^1\text{H}$ δ 7.26 ppm; $\text{CD}_2\text{H}_2\text{CN}$: ${}^1\text{H}$ δ 1.94 ppm; d_5 -DMSO: ${}^1\text{H}$ δ 2.50 ppm; d_6 -DMF: ${}^1\text{H}$ δ 2.92 ppm). ${}^{13}\text{C}$ NMR chemical shifts are referenced to solvent peak (CDCl_3 : ${}^{13}\text{C}$ δ 77.16 ppm; CD_3CN : ${}^{13}\text{C}$ δ 1.32 ppm; d_7 -DMF: ${}^{13}\text{C}$ δ 29.76 ppm). Abbreviation ABq indicates an AB quartet NMR signal. Coupling constants (J) are reported in Hertz (Hz). High resolution electrospray ionization mass spectra (HRESI-MS) were recorded on a Bruker micrOTOF-Q spectrometer. The mass spectrometer was calibrated using an external calibrant of sodium formate clusters. UV–visible absorption spectra were recorded at ambient temperature on a PerkinElmer Lambda 950 UV–vis–near-IR spectrophotometer. Infrared spectra were recorded on a Bruker Optics ALPHA FT-IR spectrometer equipped with a diamond ATR accessory. Elemental analyses were performed at the Campbell Microanalytical Laboratory, University of Otago. Photochemical reactions were carried out in a custom built “merry-go-round” UV photochemical reactor (University of Otago, Dunedin, New Zealand), containing six UV–C lamps located symmetrically around the perimeter of the photoreactor that emitted monochromatic 254 nm radiation (Rayonet RPR-2537A, Southern New England Ultraviolet Co., Branford, CT).³⁸ A fan was used to maintain the temperature of the photoreactor at 35 °C during irradiation.

$[\text{Pd}(\mathbf{4a})_2](\text{BF}_4)_2$ (5a**).** A solution of ligand **4a** (96 mg, 0.43 mmol) in acetone (5 mL) was added to a solution of $[\text{Pd}(\text{CH}_3\text{CN})_4](\text{BF}_4)_2$ (95 mg, 0.21 mmol) in acetonitrile (2 mL). The resulting pale yellow solution was stirred for 1 h, and an off-white solid precipitated after this time. The reaction mixture was cooled to -4 °C and the precipitate (complex **5a**) was collected by filtration, washed with cold acetonitrile and then diethyl ether, and dried under vacuum. Yield: 131 mg (85%). Pale yellow crystals of **5a** suitable for X-ray crystallographic analysis were obtained by vapor diffusion of methanol into a DMSO solution of **5a**. Anal. Calcd (%) for $\text{C}_{26}\text{H}_{20}\text{B}_2\text{F}_8\text{N}_8\text{Pd}$: C 43.10, H 2.78, N 15.47; found: C 42.74, H 2.92, N 15.03. ${}^1\text{H}$ NMR (400 MHz, d_7 -DMF) δ : 10.71 (s, 1H, H_c), 10.01 (dd, ${}^3J = 5.7$ Hz, ${}^4J = 1.1$ Hz, 1H, H_a), 9.05 (td, ${}^3J = 8.1$ Hz, ${}^4J = 1.4$ Hz, 1H, H_c), 8.93 (d, ${}^3J = 8.0$ Hz, 1H, H_d), 8.46 (ddd, ${}^3J = 7.3$, 5.9 Hz, ${}^4J = 1.2$ Hz, 1H, H_b), 8.31 (dd, ${}^3J = 7.9$ Hz, ${}^4J = 1.5$ Hz, 2H, H_f), 7.67–7.75 (m, 3H, H_g , H_h). ${}^1\text{H}$ NMR (400 MHz, CD_3NO_2) δ : 10.02 (dd, ${}^3J = 5.8$ Hz, ${}^4J = 1.1$ Hz, 1H, H_a), 9.56 (s, 1H, H_c), 8.79 (td, ${}^3J = 8.1$ Hz, ${}^4J = 1.4$ Hz, 1H, H_c), 8.50–8.54 (m, 1H, H_d), 8.23 (ddd, ${}^3J = 7.5$, 5.9 Hz, ${}^4J = 1.2$ Hz, 1H, H_b), 8.16–8.21 (m, 2H, H_f), 7.62–7.74 (m, 3H, H_g , H_h). ${}^{13}\text{C}$ NMR (100 MHz, d_7 -DMF) δ : 150.3, 149.6, 146.7, 131.2, 130.0, 128.1, 127.5, 126.7, 124.7, 115.8, 110.1. HRESI-MS (DMF): m/z calcd for $\text{C}_{26}\text{H}_{21}\text{N}_8\text{Pd}^+$: 551.0928 $[\text{Pd}(\mathbf{4a})_2 + \text{H}]^+$; found: 551.0940 (95%), m/z calcd for $\text{C}_{26}\text{H}_{20}\text{N}_8\text{Pd}^{2+}$: 275.0422 $[\text{Pd}(\mathbf{4a})_2]^{2+}$; found: 275.0435 (32%). UV–vis (DMF) λ_{max} ($\epsilon/\text{M}^{-1}\text{cm}^{-1}$) = 289 (34200) nm. IR (ATR): $\nu = 3127, 3092, 1038$ (s, BF_4^-) cm^{-1} .

$[\text{Pd}(\mathbf{4b})_2](\text{BF}_4)_2 \cdot 1.5\text{CH}_3\text{CN}$ (5b**·1.5 CH_3CN).** A solution of ligand **4b** (96 mg, 0.43 mmol) in acetonitrile (3 mL) was added to a solution of $[\text{Pd}(\text{CH}_3\text{CN})_4](\text{BF}_4)_2$ (90 mg, 0.20 mmol) in acetonitrile (2 mL). The resulting pale yellow solution was stirred for 1 h, and an off-white solid precipitated after this time. The reaction mixture was cooled to -4 °C and the precipitate (complex **5b**·1.5 CH_3CN) was collected by filtration, washed with diethyl ether, and dried under vacuum. Yield: 126 mg (76%). Pale yellow crystals of **5b**·2 CH_3CN suitable for X-ray crystallographic analysis were obtained by vapor diffusion of diethyl

ether into a DMF solution of **5b**-2CH₃CN. Anal. Calcd (%) for C₃₁H_{28.5}B₂F₈N_{9.5}Pd: C 45.73, H 3.53, N 16.34; found: C 45.80, H 3.56, N 16.52. ¹H NMR (400 MHz, *d*₇-DMF) δ: 9.95 (s, 1H, H_e), 9.78 (d, ³J = 5.8 Hz, 1H, H_a), 8.89–8.98 (m, 2H, H_c, H_d), 8.29 (td, ³J = 5.5 Hz, ⁴J = 3.9 Hz, 1H, H_b), 7.51 (d, ³J = 7.1 Hz, 2H, H_g), 7.45 (t, ³J = 7.5, 2H, H_h), 7.37 (t, ³J = 7.2, 1H, H_i), 4.51 (s, 2H, H_f). ¹³C NMR (100 MHz, *d*₇-DMF) δ: 150.6, 149.7, 146.5, 137.5, 129.3, 129.2, 127.5, 127.4, 126.8, 115.9, 110.1, 31.8. HRESI-MS (CH₃CN): *m/z* calcd for C₂₈H₂₄FN₈Pd⁺: 597.1148 [Pd(**4b**)₂ + F]⁺; found: 597.1153 (76%), *m/z* calcd for C₂₈H₂₄N₈Pd²⁺: 289.0579 [Pd(**4b**)₂]²⁺; found: 289.0583 (100%). UV-vis (DMF): λ_{max} (ε/M⁻¹ cm⁻¹) = 273 (31300) nm. IR (ATR): ν = 3142, 3048, 1048 (s, BF₄⁻) cm⁻¹.

[Pt(**4a**)Cl₂] (**6a**). To a mixture of *cis*-[Pt(DMSO)₂Cl₂] (145 mg, 0.343 mmol) and ligand **4a** (85 mg, 0.38 mmol) was added methanol (15 mL). The resulting mixture was refluxed for 45 min. Complex **6a** precipitated as a yellow solid, which was collected by filtration, washed with methanol, then diethyl ether, and dried under vacuum. Yield: 141 mg (84%). Yellow crystals of **6a** suitable for X-ray crystallographic analysis were obtained by vapor diffusion of diethyl ether into a DMF solution of **6a**. Anal. Calcd (%) for C₁₃H₁₀Cl₂N₄Pt: C 31.98, H 2.06, N 11.48; found: C 32.08, H 1.97, N 11.47. ¹H NMR (400 MHz, *d*₇-DMF) δ: 10.33 (s, 1H, H_e), 9.49 (dd, ³J = 5.9 Hz, ⁴J = 1.4 Hz, 1H, H_a), 8.72 (td, ³J = 8.0 Hz, ⁴J = 1.5 Hz, 1H, H_c), 8.56 (d, ³J = 8.3 Hz, 1H, H_d), 7.92–8.09 (m, 3H, H_b, H_f), 7.58–7.65 (m, 2H, H_g), 7.51–7.58 (m, 1H, H_h). ¹³C NMR (100 MHz, *d*₇-DMF) δ: 148.8, 148.4, 148.0, 143.6, 130.6, 130.1, 129.1, 126.7, 126.5, 122.4, 114.8. HRESI-MS (DMF): *m/z* calcd for C₁₃H₁₀Cl₂N₄NaPt⁺: 509.9823 [6a + Na]⁺; found: 509.9800 (100%). UV-vis (DMF): λ_{max} (ε/M⁻¹ cm⁻¹) = 366 (4170) nm. IR (ATR): ν = 3086, 1614, 1502, 1478, 1454, 1086, 761 cm⁻¹.

[Pt(**4b**)Cl₂] (**6b**). To a mixture of *cis*-[Pt(DMSO)₂Cl₂] (654 mg, 1.55 mmol) and ligand **4b** (401 mg, 1.70 mmol) was added methanol (45 mL). The resulting mixture was refluxed for 45 min. Complex **6b** precipitated as a yellow solid, which was collected by filtration, washed with methanol, then diethyl ether, and dried under vacuum. Yield: 595 mg (76%). Yellow crystals of **6b** suitable for X-ray crystallographic analysis were obtained by vapor diffusion of diisopropyl ether into a DMF solution of **6b**. Anal. Calcd (%) for C₁₄H₁₂Cl₂N₄Pt: C 33.48, H 2.41, N 11.16; found: C 33.63, H 2.33, N 11.07. ¹H NMR (400 MHz, *d*₇-DMF) δ: 9.57 (s, 1H, H_e), 9.45 (ddd, ³J = 5.9 Hz, ⁴J = 1.5 Hz, ⁵J = 0.6 Hz, 1H, H_a), 8.63 (ddd, ³J = 8.9, 7.5 Hz, ⁴J = 1.5 Hz, 1H, H_c), 8.57 (ddd, ³J = 8.3 Hz, ⁴J = 1.4 Hz, ⁵J = 0.6 Hz, 1H, H_d), 7.93 (ddd, ³J = 7.4, 5.9 Hz, ⁴J = 1.4 Hz, 1H, H_b), 7.34–7.43 (m, 4H, H_g, H_h), 7.26–7.33 (m, 1H, H_i), 4.29 (s, 2H, H_f). ¹³C NMR (100 MHz, *d*₇-DMF) δ: 149.8, 148.5, 147.9, 143.4, 138.4, 129.5, 129.4, 127.5, 127.5, 124.3, 114.8, 32.3. HRESI-MS (DMF): *m/z* calcd for C₂₈H₂₄Cl₂N₈Pt⁺: 702.1456 [Pt(**4b**)₂ + Cl]⁺; found: 702.1425 (100%), *m/z* calcd for C₁₄H₁₂Cl₂N₄NaPt⁺: 523.9980 [6b + Na]⁺; found: 523.9997 (34%). UV-vis (DMF): λ_{max} (ε/M⁻¹ cm⁻¹) = 363 (4530) nm. IR (ATR): ν = 3100, 3050, 1617, 1496, 1456, 1069, 760, 737, 709 cm⁻¹.

[Re(**4a**)(CO)₃Cl]·0.5CH₃OH (**7a**·0.5CH₃OH). Ligand **4a** (77 mg, 0.35 mmol) and [Re(CO)₃Cl] (123 mg, 0.34 mmol) were suspended in methanol (20 mL). The mixture was refluxed overnight, and a yellow solid precipitated after this time. The reaction mixture was reduced to approximately 1 mL and then cooled to 4 °C. The resulting yellow precipitate was collected by filtration, washed with ice-cold methanol, then diethyl ether, and dried under vacuum. Yield: 164 mg (89%). Yellow crystals of **7a** suitable for X-ray crystallographic analysis were obtained by vapor diffusion of diethyl ether into a DMF solution of **7a**·0.5CH₃OH. Anal. Calcd (%) for C₁₆H₁₂ClN₄O_{3.5}Re: C 36.43, H 2.22, N 10.30; found: C 36.89, H 2.36, N 10.44. ¹H NMR (400 MHz, *d*₇-DMF) δ: 10.27 (s, 1H, H_e), 9.16–9.20 (m, 1H, H_a), 8.64–8.71 (m, 2H, H_c, H_d), 8.05–8.10 (m, 2H, H_f), 7.92 (ddd, ³J = 6.6, 5.6 Hz, ⁴J = 2.2 Hz, 1H, H_b), 7.60–7.66 (m, 2H, H_g), 7.52–7.59 (m, 1H, H_h). ¹³C NMR (100 MHz, *d*₇-DMF) δ: 153.1, 150.4, 148.2, 143.7, 130.2, 129.8, 128.4, 127.1, 126.1, 122.2, 115.3. HRESI-MS (CH₃CN): *m/z* calcd for C₁₆H₁₀ClN₄NaO₃Re⁺: 550.9878 [7a + Na]⁺; found: 550.9882 (100%). UV-vis (DMF): λ_{max} (ε/M⁻¹ cm⁻¹) = 359 (4300) nm. IR (ATR): ν = 3136, 2026 (w, CO), 1906 (w, CO), 1889 (w, CO) cm⁻¹.

[Re(**4b**)(CO)₃Cl]·0.5CH₃OH (**7b**·0.5CH₃OH). Ligand **4b** (92 mg, 0.39 mmol) and [Re(CO)₃Cl] (138 mg, 0.38 mmol) were suspended in methanol (20 mL). The mixture was refluxed overnight. The reaction mixture was concentrated to approximately 1 mL and then cooled to 4 °C. The resulting yellow precipitate was collected by filtration, washed with ice-cold methanol, ice-cold diethyl ether and petroleum ether (40–60 °C), and dried under vacuum. Yield: 176 mg (83%). Yellow crystals of **7b**·CH₂Cl₂ suitable for X-ray crystallographic analysis were obtained by vapor diffusion of diethyl ether into a CH₂Cl₂ solution of **7b**·0.5CH₃OH. Anal. Calcd (%) for C_{17.5}H₁₄ClN₄O_{3.5}Re: C 37.67, H 2.53, N 10.04; found: C 37.87, H 2.64, N 10.02. ¹H NMR (400 MHz, *d*₇-DMF) δ: 9.52 (s, 1H, H_e), 9.12 (ddd, ³J = 5.5 Hz, ⁴J = 1.5 Hz, ⁵J = 0.6 Hz, 1H, H_a), 8.69 (d, ³J = 8.3 Hz, 1H, H_d), 8.58 (ddd, ³J = 8.4, 7.6 Hz, ⁴J = 1.6 Hz, 1H, H_c), 7.86 (ddd, ³J = 7.5, 5.6 Hz, ⁴J = 1.2 Hz, 1H, H_b), 7.36–7.45 (m, 4H, H_g, H_h), 7.28–7.34 (m, 1H, H_i), 4.31 (s, 2H, H_f). ¹³C NMR (100 MHz, *d*₇-DMF) δ: 153.0, 151.4, 148.2, 143.5, 138.1, 129.2, 129.1, 127.2, 126.8, 124.1, 115.3, 31.6. HRESI-MS (CH₃CN): *m/z* calcd for C₁₇H₁₂ClN₄NaO₃Re⁺: 565.0031 [7b + Na]⁺; found: 565.0039 (100%). UV-vis (DMF): λ_{max} (ε/M⁻¹ cm⁻¹) = 358 (4200) nm. IR (ATR): ν = 3125, 2026 (w, CO), 1941 (w, CO), 1884 (w, CO) cm⁻¹.

[Ru(bpy)₂(**4a**)](PF₆)₂ (**8a**). Ethanol (10 mL) was added to a mixture of *cis*-[Ru(bpy)₂Cl₂] (137 mg, 0.28 mmol) and ligand **4a** (67 mg, 0.30 mmol). The mixture was stirred at room temperature for 5 min and the resulting solution was degassed with argon. The solution was heated at 125 °C in a microwave (200 W) for 1 h. During irradiation the solution became orange-yellow. After cooling the solution to room temperature, a saturated aqueous solution of NH₄PF₆ (15 mL) was added dropwise. The crude product precipitated as an orange-yellow solid immediately. The mixture was stirred for 10 min, and the orange-yellow precipitate was collected by filtration. The crude product was dissolved in acetone and the resulting solution was added dropwise to a stirred diisopropyl ether solution. Complex **8a** precipitated as an orange-yellow solid and was collected by filtration, washed with ice-cold water, then ice-cold ethanol, and finally with diethyl ether, and dried under vacuum. Yield: 193 mg (74%). Orange-yellow crystals of **8a**·2CH₂Cl₂ suitable for X-ray crystallographic analysis were obtained by vapor diffusion of diisopropyl ether into a dichloromethane solution of **8a**. Anal. Calcd (%) for C₃₃H₂₆F₁₂N₈P₂Ru: C 42.82, H 2.83, N 12.11; found: C 42.96, H 2.87, N 11.82. ¹H NMR (500 MHz, CD₃CN) δ: 9.36 (s, 1H, H_e), 8.46–8.55 (m, 4H, bpyH), 8.21–8.26 (m, 1H, H_c), 8.18 (d, ³J = 8.0 Hz, 1H, H_d), 8.06–8.14 (m, 4H, bpyH), 7.89 (ddd, ³J = 5.6 Hz, ⁴J = 1.4 Hz, ⁵J = 0.7 Hz, 1H, bpyH), 7.86 (ddd, ³J = 5.6 Hz, ⁴J = 1.3 Hz, ⁵J = 0.6 Hz, 1H, bpyH), 7.81 (ddd, ³J = 5.6 Hz, ⁴J = 1.3 Hz, ⁵J = 0.6 Hz, 1H, bpyH), 7.76 (ddd, ³J = 5.6 Hz, ⁴J = 1.4 Hz, ⁵J = 0.7 Hz, 1H, bpyH), 7.71–7.75 (m, 3H, H_g, H_f), 7.38–7.51 (m, 8H, H_b, H_g, H_h, bpyH). ¹H NMR (400 MHz, *d*₇-DMF) δ: 10.39 (s, 1H, H_e), 8.92–9.04 (m, 4H), 8.75 (d, ³J = 8.1 Hz, 1H), 8.50 (t, ³J = 7.4 Hz, 1H), 8.23–8.37 (m, 6H), 8.12 (d, ³J = 5.6 Hz, 2H), 8.07–8.10 (m, 1H), 7.80 (d, ³J = 6.9 Hz, 2H), 7.69–7.76 (m, 2H), 7.62–7.69 (m, 3H), 7.43–7.56 (m, 3H). ¹³C NMR (125 MHz, CD₃CN) δ: 158.4, 158.2, 158.1, 157.7, 153.5, 153.5, 153.1, 153.0, 152.4, 151.6, 149.6, 141.7, 139.5, 139.4, 139.4, 139.2, 130.8, 130.3, 129.1, 129.0, 128.7, 128.6, 128.0, 127.3, 126.7, 125.5, 125.4, 125.1, 124.8, 122.7, 115.6. HRESI-MS (CH₂Cl₂): *m/z* calcd for C₃₃H₂₆F₆N₈PRu⁺: 781.0968 [Ru(bpy)₂(**4a**) + (PF₆)⁺]; found: 781.0909 (23%), *m/z* calcd for C₃₃H₂₆N₈Ru²⁺: 318.0661 [Ru(bpy)₂(**4a**)]²⁺; found: 318.0652 (100%), *m/z* calcd for C₃₃H₂₆N₆Ru²⁺: 304.0630 [Ru(bpy)₂(**4a**) – N₂]²⁺; found: 304.0621 (74%). UV-vis (CH₂Cl₂): λ_{max} (ε/M⁻¹ cm⁻¹) = 424 (17400) nm. IR (ATR): ν = 3181, 3087, 1709, 1605, 1491, 1467, 1446, 1222, 1062, 833 (s, PF₆⁻), 763, 731, 699, 556 (m, PF₆⁻) cm⁻¹.

[Ru(bpy)₂(**4b**)](PF₆)₂ (**8b**). Ethanol (10 mL) was added to a mixture of *cis*-[Ru(bpy)₂Cl₂] (129 mg, 0.27 mmol) and ligand **4b** (68 mg, 0.28 mmol). The mixture was stirred at room temperature for 5 min and the resulting solution was degassed with argon. The solution was heated at 125 °C in a microwave (200 W) for 1 h. During this time the solution became orange-yellow. After cooling the solution to room temperature, a saturated aqueous solution of NH₄PF₆ (15 mL) was added dropwise. Complex **8b** precipitated as an orange-yellow solid immediately. The mixture was stirred for 10 min, and the orange-

yellow precipitate was collected by filtration; washed with ice-cold water, then ice-cold ethanol, and finally with diethyl ether; and dried under vacuum. Yield: 197 mg (78%). Vapor diffusion of diisopropyl ether and diethyl ether into an acetonitrile solution of **8b** gave orange crystals of **8b**·2CH₃CN and **8b**·CH₃CN, respectively, suitable for X-ray crystallographic analysis. Anal. Calcd (%) for C₃₄H₂₈F₁₂N₈P₂Ru: C 43.46, H 3.00, N 11.93; found: C 43.29, H 2.91, N 11.87. ¹H NMR (500 MHz, CD₃CN) δ: 8.69 (s, 1H, H_c), 8.42–8.54 (m, 4H, bpyH), 8.15 (ddd, ³J = 8.3, 7.6 Hz, ⁴J = 1.5 Hz, 1H, H_c), 8.03–8.13 (m, 5H, H_d, bpyH), 7.83 (ddd, ³J = 5.6 Hz, ⁴J = 1.5 Hz, ⁵J = 0.7 Hz, 1H, bpyH), 7.79 (ddd, ³J = 5.7 Hz, ⁴J = 1.5 Hz, ⁵J = 0.7 Hz, 1H, bpyH), 7.77 (ddd, ³J = 5.6 Hz, ⁴J = 1.5 Hz, ⁵J = 0.7 Hz, 1H, bpyH), 7.71 (ddd, ³J = 5.7 Hz, ⁴J = 1.4 Hz, ⁵J = 0.7 Hz, 1H, bpyH), 7.68 (ddd, ³J = 5.7 Hz, ⁴J = 1.5 Hz, ⁵J = 0.7 Hz, 1H, H_a), 7.40–7.48 (m, 4H, H_b, bpyH), 7.37 (ddd, ³J = 7.6, 5.7 Hz, ⁴J = 1.3 Hz, 1H, bpyH), 7.29–7.34 (m, 2H, H_b), 7.25–7.29 (m, 1H, H_i), 7.14–7.19 (m, 2H, H_g), 4.07 and 4.03 (ABq, ²J = 16.2 Hz, 2H, H_f). ¹H NMR (400 MHz, d₇-DMF) δ: 9.59 (s, 1H, H_c), 8.88–9.04 (m, 4H), 8.76 (d, ³J = 8.1 Hz, 1H), 8.42 (t, ³J = 8.2 Hz, ⁴J = 1.2 Hz, 1H), 8.23–8.36 (m, 4H), 8.21 (d, ³J = 4.7 Hz, 1H), 8.10–8.15 (m, 2H), 8.04–8.09 (m, 2H), 7.57–7.71 (m, 5H), 7.24–7.38 (m, 3H), 7.15–7.23 (m, 2H), 4.13 and 4.09 (ABq, ²J = 16.4 ± 0.2 Hz, 2H, H_f). ¹³C NMR (125 MHz, CD₃CN) δ: 158.4, 158.1, 158.1, 157.7, 153.4, 153.4, 153.1, 153.0, 152.3, 152.2, 149.7, 141.5, 139.4, 139.4, 139.3, 139.2, 138.4, 129.8, 129.6, 128.9, 128.6, 128.5, 128.0, 127.9, 127.1, 125.4, 125.4, 125.1, 124.9, 124.7, 115.7, 32.4. HRESI-MS (CH₂Cl₂): *m/z* calcd for C₃₄H₂₈F₆N₈PRu⁺: 795.1125 [Ru(bpy)₂(**4b**) + (PF₆)⁻]; found: 795.1087 (18%), *m/z* calcd for C₃₄H₂₈N₈Ru²⁺: 325.0739 [Ru(bpy)₂(**4b**)²⁺]; found: 325.0714 (100%), *m/z* calcd for C₃₄H₂₈N₆Ru²⁺: 311.0708 [Ru(bpy)₂(**4b**) - N₂]²⁺; found: 311.0687 (24%), *m/z* calcd for C₂₆H₂₀N₆Ru²⁺: 259.0394 [Ru(bpy)₂(NC₃H₄-N≡C)]²⁺; found: 259.0360 (20%). UV-vis (CH₂Cl₂): λ_{max} (ε/M⁻¹ cm⁻¹) = 421 (16000) nm. IR (ATR): ν = 3153, 3087, 1604, 1547, 1494, 1467, 1447, 1063, 830 (s, PF₆⁻), 763, 731, 713, 556 (m, PF₆⁻) cm⁻¹.

X-ray Crystallography. X-ray data for **5a**, **5b**·2CH₃CN, **6a**, **6b**, **7a**, **7b**·CH₂Cl₂, **8a**·2CH₂Cl₂, **8b**·2CH₃CN (polymorph 1), **8b**·CH₃CN (polymorph 2), **12a**·CH₃CN, and **12b**·0.5(C₄H₁₀O) were collected at 100 K on an Agilent Technologies Supernova system using Cu Kα radiation with exposures over 1.0°. X-ray data were treated using CrysAlisPro³⁹ software. X-ray crystal structures were solved using SIR-97⁴⁰ and weighted full-matrix refinement on F² was carried out using SHELXL-97⁴¹ running within the WinGX⁴² package. The CCDC reference numbers for these compounds are 1013165-1013174 and 1014293.

Data Refinement Details for 5a, 5b·2CH₃CN, 6a, 6b, 7b·CH₂Cl₂, and 8b·2CH₃CN (Polymorph 1). All non-hydrogen atoms were refined anisotropically. Hydrogen atoms were placed in calculated positions and refined using a riding model.

Data Refinement Details for 7a. All non-hydrogen atoms were refined anisotropically. Hydrogen atoms were placed in calculated positions and refined using a riding model. Atoms Cl1, C1, C16, N2, O2, and O3 became nonpositive definites when refined anisotropically and were modeled with the ISOR command. The ellipsoids of atoms C2, C7, C8, C12, C14, and O1 became slightly elongated or flattened when refined anisotropically. These atoms were modeled with the ISOR command. The triazolyl ring was modeled with the SIMU command. The pyridyl and phenyl rings were modeled with a combination of the SIMU and AFIX 66 commands.

The crystal lattice contained a smaller amount of diffuse electron density that could not be appropriately modeled. The SQUEEZE routine within PLATON was employed to resolve this problem, resulting in a void electrons count of 128 that were assigned to two disordered solvent dimethylformamide and four water molecules (120 electrons in total).

Data Refinement Details for 8a·2CH₂Cl₂. All non-hydrogen atoms were refined anisotropically. Hydrogen atoms were placed in calculated positions and refined using a riding model. There are two solvent dichloromethane molecules one of which was disordered. The disordered dichloromethane molecule was modeled with the PART command and refined over two sites with 50% occupancy. The DFIX

command was used to model the C–Cl (1.77 Å) and Cl–Cl (2.92 Å) distances while the ISOR command was used to model atoms C34, C35, Cl1, Cl3, and Cl4 in the disordered dichloromethane molecules.

Data Refinement Details for 8b·CH₃CN (Polymorph 2). All non-hydrogen atoms were refined anisotropically. Hydrogen atoms were placed in calculated positions and refined using a riding model. The PF₆⁻ anion consists of P2 and F7 through F12 was slightly disordered. The fluorine atoms F9 through F12 were modeled with the ISOR command.

Both solvent acetonitrile molecules were disordered. The ISOR command was employed to model atoms N99 and C98 in one of the acetonitrile molecules. The other acetonitrile molecule is highly disordered and could not be appropriately modeled. The SQUEEZE routine within PLATON was employed to resolve this problem, resulting in a void electrons count of 40 that were assigned to two disordered acetonitrile molecules (44 electrons in total).

Data Refinement Details for 12a·CH₃CN. All non-hydrogen atoms were refined anisotropically. Hydrogen atoms were placed in calculated positions and refined using a riding model. The solvent acetonitrile molecule was slightly disordered. The ISOR command was employed to model atoms N99, C99, and C98, and the DFIX command was used to model the N99–C99 (1.14 Å) and C99–C98 (1.46 Å) distances. The PF₆⁻ anion consists of P2 and F7 through F12 is slightly disordered. The ISOR command was employed to model atoms P2 and F8 through F12. The ellipsoids of atoms C11 through C15, C17 through C20 and C29 through C33 were slightly elongated when refined anisotropically. The ISOR command was used to model these atoms.

Data Refinement Details for 12b·0.5(C₄H₁₀O). All non-hydrogen atoms were refined anisotropically. Hydrogen atoms were placed in calculated positions and refined using a riding model. One of the PF₆⁻ anions was disordered over two sites. It was modeled with the PART command with occupancies of 65% (P4 and F19 to F24) and 35% (P5 and F25 to F30) over two sites. The DFIX commands were used to fix the P–F (1.60 Å) and F–F (2.26 Å) distances within the disordered PF₆⁻. The ISOR command was used to model fluorine atoms F23, F25, F26, F27, F29, and F30.

Electrochemistry. Cyclic and differential pulse voltammetric experiments in DMF were performed at 20 °C on solutions degassed with argon. A three-electrode cell was used with a Cypress Systems glassy carbon working electrode (1.4 mm diameter), a Ag/AgCl reference electrode, and a platinum wire auxiliary electrode. The solutions were approximately 1 mM of electroactive material and 0.10 M of tetrabutylammonium hexafluorophosphate (Bu₄NPF₆) as the supporting electrolyte. Voltammograms were recorded with a Powerlab/4sp computer-controlled potentiostat. Potentials are referenced to the reversible formal potential (taken as E° = 0.00 V) for the decamethylferrocenium/decamethylferrocene ([Fc*]⁺⁰) couple,¹⁵ where E° was calculated from the average of the oxidation and reduction peak potentials. Under the same conditions, E° calculated for ferrocenium/ferrocene couple ([FcH]⁺⁰) was 0.48 V versus [Fc*]⁺⁰.¹⁶

Physical Measurements. Fourier-transform Raman (FT-Raman) spectra were obtained from solid samples using a Bruker Equinox-55 FT-interferometer with an FRA106/5 Raman accessory and D418T liquid-nitrogen-cooled Germanium detector with 1064 nm excitation provided by a Nd:YAG laser. Raman spectra with 830 nm excitation were recorded on an i-Raman spectrometer (B&W Tek Inc.) using solid samples.

Electronic absorption spectra were recorded on an Ocean Optics USB2000. Steady-state emission spectra were recorded on a Princeton Instruments SP2150i spectrograph with 300 groove mm⁻¹ grating and Pixis 110 B CCD. A krypton-ion laser (Innova I-302, Coherent, Inc.) provided excitation at 350.7 nm of 12 mW. [Ru(bpy)₃]Cl₂ was used as a quantum yield standard.⁴³ Quantum yield errors are ±10%. Excited-state lifetimes were obtained from transient emission and absorption spectra acquired with an Edinburgh Instruments LP920 flash photolysis system using the 354.7 nm pulsed output of a Brilliant (Quintel) Nd:YAG laser for excitation.

Resonance Raman spectra were recorded using a previously described setup.⁴⁴ Solutions were 1–5 mM in spectroscopic grade solvents. Excitation wavelengths of 350.7, 356.4, 406.7, and 413.1 nm were obtained from a krypton-ion laser (Innova I-302, Coherent Inc.), 457.9 nm from a diode-pumped solid-state laser (Cobolt Inc.), and 363.7 nm from an argon-ion laser (Innova Sabre 20, Coherent Inc.). Laser power at the sample was about 30 mW. The incident beam and collection lens were arranged in a 135° backscattering geometry to reduce loss of Raman intensity by self-absorption.

Computational Methods. All density functional theory (DFT) calculations were performed using Gaussian 09.⁴⁵ The LANL2DZ⁴⁶ effective core potential basis set was used for all metals and the 6-31G(d) basis set for all other atoms. The B3LYP⁴⁷ functional was used to optimize the rhenium and platinum structures and to simulate Raman spectra with the polarizable continuum model (PCM)⁴⁸ in DMF. Time-dependent DFT calculations for the rhenium complexes used the Perdew–Burke–Ernzerhof exchange–correlation (PBE0)²¹ functional with PCM in CH₂Cl₂. Ligand competition calculations for the Pd complexes were performed with the B3LYP functional in the gas phase. The PBE0 functional was used for modeling all Ru complexes. PCM solvation in dichloromethane was used for Ru complexes except in modeling solvolysis where CH₃CN was used. The triplet state calculations for Ru complexes were based on a procedure from Persson and co-workers.³⁴ The singlet ground state was initially optimized. This structure was used to optimize the ³MLCT state using unrestricted DFT. The ³MC states were optimized with unrestricted DFT by initially elongating two Ru–N bonds of the ³MLCT structure to about 2.4 Å.

■ ASSOCIATED CONTENT

● Supporting Information

Reaction scheme, supplementary experimental section, selected NMR spectra, mass spectra, crystal structures, cyclic voltammograms, UV–vis spectra, Raman spectra, emission spectra, DFT calculations, .xyz files, and CIFs giving crystallographic data for **5a**, **5b**-2CH₃CN, **6a**, **6b**, **7a**, **7b**-CH₂Cl₂, **8a**-2CH₂Cl₂, **8b**-2CH₃CN (polymorph 1), **8b**-CH₃CN (polymorph 2), **12a**-CH₃CN, **12b**-0.5(C₄H₁₀O), **14**, **16a**-0.5CH₂Cl₂, **16b**, and **17b**. This material is available free of charge via the Internet at <http://pubs.acs.org>.

■ AUTHOR INFORMATION

Corresponding Author

*E-mail: jcrowley@chemistry.otago.ac.nz. Fax: +64 3 479 7906. Phone: +64 3 479 7731.

Author Contributions

The manuscript was written through contributions of all authors. All authors have given approval to the final version of the manuscript.

Notes

The authors declare no competing financial interest.

■ ACKNOWLEDGMENTS

This work was supported by the Department of Chemistry, University of Otago. W.K.C.L., J.R.C., and G.S.H. thank the University of Otago for doctoral scholarships. C.J.M. thanks the NZ Ministry of Business, Innovation and Employment Science Investment Fund (Grant no. UOOX1206), for financial support.

■ REFERENCES

(1) (a) Rostovtsev, V. V.; Green, L. G.; Fokin, V. V.; Sharpless, K. B. *Angew. Chem., Int. Ed.* **2002**, *41*, 2596–2599. (b) Tornøe, C. W.; Christensen, C.; Meldal, M. *J. Org. Chem.* **2002**, *67*, 3057–3064.

(2) (a) Schulze, B.; Schubert, U. S. *Chem. Soc. Rev.* **2014**, *43*, 2522–2571. (b) Crowley, J. D.; McMorran, D. A. *Top. Heterocycl. Chem.* **2012**, *28*, 31–83. (c) Schweinfurth, D.; Deibel, N.; Weisser, F.; Sarkar, B. *Nachr. Chem.* **2011**, *59*, 937–941. (d) Struthers, H.; Mindt, T. L.; Schibli, R. *Dalton Trans.* **2010**, *39*, 675–696.

(3) (a) Vellas, S. K.; Lewis, J. E. M.; Shankar, M.; Sagatova, A.; Tyndall, J. D. A.; Monk, B. C.; Fitchett, C. M.; Hanton, L. R.; Crowley, J. D. *Molecules* **2013**, *18*, 6383–6407. (b) Pokharel, U. R.; Fronczek, F. R.; Maverick, A. W. *Dalton Trans.* **2013**, *42*, 14064–14067. (c) Stevenson, K. A.; Melan, C. F. C.; Fleischel, O.; Wang, R.; Petitjean, A. *Cryst. Growth Des.* **2012**, *12*, 5169–5173. (d) Crowley, J. D.; Bandoen, P. H. *Dalton Trans.* **2010**, *39*, 612–623.

(4) (a) Potier, J.; Menuel, S.; Rousseau, J.; Tumkevicius, S.; Hapiot, F.; Monflier, E. *Appl. Catal., A* **2014**, *479*, 1–8. (b) Zhang, G.; Luan, Y.; Han, X.; Wang, Y.; Wen, X.; Ding, C.; Gao, J. *Green Chem.* **2013**, *15*, 2081–2085. (c) Wang, D.; Denux, D.; Ruiz, J.; Astruc, D. *Adv. Synth. Catal.* **2013**, *355*, 129–142. (d) Kong, F.; Zhou, C.; Wang, J.; Yu, Z.; Wang, R. *ChemPlusChem.* **2013**, *78*, 536–545. (e) Dickschat, A. T.; Surmiak, S.; Studer, A. *Synlett* **2013**, *24*, 1523–1528. (f) Dickschat, A. T.; Behrends, F.; Surmiak, S.; Weiss, M.; Eckert, H.; Studer, A. *Chem. Commun.* **2013**, *49*, 2195–2197. (g) Zhang, G.; Wang, Y.; Wen, X.; Ding, C.; Li, Y. *Chem. Commun.* **2012**, *48*, 2979–2981. (h) Schweinfurth, D.; Su, C.-Y.; Wei, S.-C.; Braunstein, P.; Sarkar, B. *Dalton Trans.* **2012**, *41*, 12984–12990. (i) Djernes, K. E.; Padilla, M.; Mettry, M.; Young, M. C.; Hooley, R. J. *Chem. Commun.* **2012**, *48*, 11576–11578. (j) Djernes, K. E.; Moshe, O.; Mettry, M.; Richards, D. D.; Hooley, R. J. *Org. Lett.* **2012**, *14*, 788–791. (k) Grotjahn, D. B.; Brown, D. B.; Martin, J. K.; Marelius, D. C.; Abadjian, M.-C.; Tran, H. N.; Kalyuzhny, G.; Vecchio, K. S.; Specht, Z. G.; Cortes-Llamas, S. A.; Miranda-Soto, V.; van Niekerk, C.; Moore, C. E.; Rheingold, A. L. *J. Am. Chem. Soc.* **2011**, *133*, 19024–19027. (l) Lalrempuia, R.; McDaniel, N. D.; Müller-Bunz, H.; Bernhard, S.; Albrecht, M. *Angew. Chem., Int. Ed.* **2010**, *49*, 9765–9768.

(5) (a) Hohloch, S.; Schweinfurth, D.; Sommer, M. G.; Weisser, F.; Deibel, N.; Ehret, F.; Sarkar, B. *Dalton Trans.* **2014**, *43*, 4437–4450. (b) Schweinfurth, D.; Buettner, N.; Hohloch, S.; Deibel, N.; Klein, J.; Sarkar, B. *Organometallics* **2013**, *32*, 5834–5842. (c) Romero, T.; Espinosa, A.; Tarraga, A.; Molina, P. *Supramol. Chem.* **2012**, *24*, 826–832. (d) Romero, T.; Orenes, R. A.; Espinosa, A.; Tarraga, A.; Molina, P. *Org. Chem.* **2011**, *50*, 8214–8224.

(6) (a) Schweinfurth, D.; Krzystek, J.; Schapiro, I.; Demeshko, S.; Klein, J.; Telsler, J.; Ozarowski, A.; Su, C.-Y.; Meyer, F.; Atanasov, M.; Neese, F.; Sarkar, B. *Inorg. Chem.* **2013**, *52*, 6880–6892. (b) Guha, P. M.; Phan, H.; Kinyon, J. S.; Brotherton, W. S.; Sreenath, K.; Simmons, J. T.; Wang, Z.; Clark, R. J.; Dalal, N. S.; Shatruck, M.; Zhu, L. *Inorg. Chem.* **2012**, *51*, 3465–3477.

(7) (a) Baschieri, A.; Muzzioli, S.; Fiorini, V.; Matteucci, E.; Massi, M.; Sambri, L.; Stagni, S. *Organometallics* **2014**, *33*, 6154–6164. (b) Clede, S.; Lambert, F.; Saint-Fort, R.; Plamont, M.-A.; Bertrand, H.; Vessieres, A.; Policar, C. *Chem.–Eur. J.* **2014**, *20*, 8714–8722. (c) Deepthi, S. B.; Trivedi, R.; Giribabu, L.; Sujitha, P.; Kumar, C. G. *Inorg. Chim. Acta* **2014**, *416*, 164–170. (d) Garcia, L.; Franzoni, S.; Mussi, F.; Aumont-Nicaise, M.; Bertrand, H.; Desmadril, M.; Pelosi, G.; Buschini, A.; Policar, C. *J. Inorg. Biochem.* **2014**, *135*, 40–44. (e) Yano, S.; Ohi, H.; Ashizaki, M.; Obata, M.; Mikata, Y.; Tanaka, R.; Nishioka, T.; Kinoshita, I.; Sugai, Y.; Okura, I.; Ogura, S.-i.; Czaplowska, J. A.; Gottschaldt, M.; Schubert, U. S.; Funabiki, T.; Morimoto, K.; Nakai, M. *Chem. Biodiversity* **2012**, *9*, 1903–1915. (f) Deepthi, S. B.; Trivedi, R.; Sujitha, P.; Kumar, C. G.; Sridhar, B.; Bhargava, S. K. *J. Chem. Sci.* **2012**, *124*, 1405–1413. (g) Francois, A.; Auzanneau, C.; Le Morvan, V.; Galaup, C.; Godfrey, H. S.; Marty, L.; Boulay, A.; Artigau, M.; Mestre-Voegtle, B.; Leygue, N.; Picard, C.; Coulais, Y.; Robert, J.; Benoist, E. *Dalton Trans.* **2014**, *43*, 439–450. (h) Mattson, E. C.; Unger, M.; Clede, S.; Lambert, F.; Policar, C.; Imtiaz, A.; D'Souza, R.; Hirschmugl, C. J. *Analyst* **2013**, *138*, 5610–5618. (i) Huang, R.; Langille, G.; Gill, R. K.; Li, C. M. J.; Mikata, Y.; Wong, M. Q.; Yapp, D. T.; Storr, T. *J. Biol. Inorg. Chem.* **2013**, *18*, 831–844. (j) Clede, S.; Lambert, F.; Sandt, C.; Gueroui, Z.; Refregiers, M.; Plamont, M.-A.; Dumas, P.; Vessieres, A.; Policar, C. *Chem.*

Commun. **2012**, *48*, 7729–7731. (k) Jones, M. R.; Service, E. L.; Thompson, J. R.; Wang, M. C. P.; Kimsey, I. J.; DeToma, A. S.; Ramamoorthy, A.; Lim, M. H.; Storr, T. *Metalomics* **2012**, *4*, 910–920.

(8) (a) Darmawan, N.; Yang, C.-H.; Mauro, M.; Froehlich, R.; De Cola, L.; Chang, C.-H.; Wu, Z.-J.; Tai, C.-W. *J. Mater. Chem. C* **2014**, *2*, 2569–2582. (b) Marty, L.; Francois, A.; Krachko, T.; Galaup, C.; Picard, C.; Amirkhanov, V. M.; Benoist, E. *Zh. Org. Farm. Khim.* **2013**, *11*, 67–71. (c) Wolff, M.; Munoz, L.; Francois, A.; Carrayon, C.; Seridi, A.; Saffon, N.; Picard, C.; Machura, B.; Benoist, E. *Dalton Trans.* **2013**, *42*, 7019–7031. (d) Kim, T. Y.; Elliott, A. B. S.; Shaffer, K. J.; John, M. C.; Gordon, K. C.; Crowley, J. D. *Polyhedron* **2013**, *52*, 1391–1398. (e) Obata, M.; Kitamura, A.; Mori, A.; Kameyama, C.; Czaplowska, J. A.; Tanaka, R.; Kinoshita, I.; Kusumoto, T.; Hashimoto, H.; Harada, M.; Mikata, Y.; Funabiki, T.; Yano, S. *Dalton Trans.* **2008**, 3292–3300. (f) Xiao, N.; Chen, Y.; Shen, X.; Zhang, C.; Yano, S.; Gottschaldt, M.; Schubert, U. S.; Kakuchi, T.; Satoh, T. *Polym. J.* **2013**, *45*, 216–225. (g) Mattiuzzi, A.; Marcélis, L.; Jabin, I.; Moucheron, C.; Mesmaeker, A. K.-D. *Inorg. Chem.* **2013**, *52*, 11228–11236. (h) Leigh, V.; Ghattas, W.; Lalrempuia, R.; Muller-Bunz, H.; Pryce, M. T.; Albrecht, M. *Inorg. Chem.* **2013**, *52*, 5395–5402. (i) Happ, B.; Schaefer, J.; Friebe, C.; Goerls, H.; Winter, A.; Hager, M. D.; Popp, J.; Dietzek, B.; Schubert, U. S. *Synthesis* **2012**, *44*, 2287–2294. (j) Escudero, D.; Happ, B.; Winter, A.; Hager, M. D.; Schubert, U. S.; González, L. *Chem.-Asian J.* **2012**, *7*, 667–671. (k) Mattiuzzi, A.; Jabin, I.; Moucheron, C.; Kirsch-De, M. A. *Dalton Trans.* **2011**, *40*, 7395–7402. (l) Happ, B.; Schaefer, J.; Menzel, R.; Hager, M. D.; Winter, A.; Popp, J.; Beckert, R.; Dietzek, B.; Schubert, U. S. *Macromolecules* **2011**, *44*, 6277–6287. (m) Happ, B.; Escudero, D.; Hager, M. D.; Friebe, C.; Winter, A.; Gorls, H.; Altuntas, E.; Gonzalez, L.; Schubert, U. S. *J. Org. Chem.* **2010**, *75*, 4025–4038. (n) Happ, B.; Friebe, C.; Winter, A.; Hager, M. D.; Hooogenboom, R.; Schubert, U. S. *Chem.-Asian J.* **2009**, *4*, 154–163. (o) Felici, M.; Contreras-Carballeda, P.; Vida, Y.; Smits, J. M. M.; Nolte, R. J. M.; De Cola, L.; Williams, R. M.; Feiters, M. C. *Chem.-Eur. J.* **2009**, *15*, 13124–13134. (p) Fletcher, J. T.; Bumgarner, B. J.; Engels, N. D.; Skoglund, D. A. *Organometallics* **2008**, *27*, 5430–5433. (q) Fernandez-Hernandez, J. M.; Ladouceur, S.; Shen, Y.; Iordache, A.; Wang, X.; Donato, L.; Gallagher-Duval, S.; de, A. V. M.; Slinker, J. D.; De, C. L.; Zysman-Colman, E. *J. Mater. Chem. C* **2013**, *1*, 7440–7452. (r) Zanarini, S.; Felici, M.; Valenti, G.; Marcaccio, M.; Prodi, L.; Bonacchi, S.; Contreras-Carballeda, P.; Williams, R. M.; Feiters, M. C.; Nolte, R. J. M.; De Cola, L.; Paolucci, F. *Chem.-Eur. J.* **2011**, *17*, 4640–4647. (s) Liu, S.; Muller, P.; Takase, M. K.; Swager, T. M. *Inorg. Chem.* **2011**, *50*, 7598–7609. (t) Fernandez-Hernandez, J. S. M.; Yang, C.-H.; Beltrán, J. I.; Lemaure, V.; Polo, F.; Fröhlich, R.; Cornil, J.; De Cola, L. *J. Am. Chem. Soc.* **2011**, *133*, 10543–10558. (u) Mydlak, M.; Bizzarri, C.; Hartmann, D.; Sarfert, W.; Schmid, G.; De Cola, L. *Adv. Funct. Mater.* **2010**, *20*, 1812–1820. (v) Felici, M.; Contreras-Carballeda, P.; Smits, J. M. M.; Nolte, R. J. M.; Williams, R. M.; De Cola, L.; Feiters, M. C. *Molecules* **2010**, *15*, 2039–2059.

(9) (a) Kuang, G.-C.; Michaels, H. A.; Simmons, J. T.; Clark, R. J.; Zhu, L. *J. Org. Chem.* **2010**, *75*, 6540–6548. (b) Brotherton, W. S.; Michaels, H. A.; Simmons, J. T.; Clark, R. J.; Dalal, N. S.; Zhu, L. *Org. Lett.* **2009**, *11*, 4954–4957. (c) Urankar, D.; Pevec, A.; Kosmrlj, J. *Eur. J. Inorg. Chem.* **2011**, 1921–1929. (d) Pinter, B.; Demsar, A.; Urankar, D.; De Proft, F.; Kosmrlj, J. *Polyhedron* **2011**, *30*, 2368–2373. (e) Bratsos, I.; Urankar, D.; Zangrando, E.; Genova-Kalou, P.; Kosmrlj, J.; Alessio, E.; Turel, I. *Dalton Trans.* **2011**, *40*, 5188–5199. (f) Urankar, D.; Pinter, B.; Pevec, A.; De Proft, F.; Turel, I.; Kosmrlj, J. *Inorg. Chem.* **2010**, *49*, 4820–4829. (g) Urankar, D.; Pevec, A.; Turel, I.; Kosmrlj, J. *Cryst. Growth Des.* **2010**, *10*, 4920–4927. (h) Anderson, C. B.; Elliott, A. B. S.; McAdam, C. J.; Gordon, K. C.; Crowley, J. D. *Organometallics* **2013**, *32*, 788–797. (i) Kilpin, K. J.; Gavey, E. L.; McAdam, C. J.; Anderson, C. B.; Lind, S. J.; Keep, C. C.; Gordon, K. C.; Crowley, J. D. *Inorg. Chem.* **2011**, *50*, 6334–6346. (j) Kilpin, K. J.; Crowley, J. D. *Polyhedron* **2010**, *29*, 3111–3117. (k) Crowley, J. D.; Gavey, E. L. *Dalton Trans.* **2010**, *39*, 4035–4037.

(l) Crowley, J. D.; Bandeen, P. H.; Hanton, L. R. *Polyhedron* **2010**, *29*, 70–83.

(10) (a) Bertrand, H. C.; Clede, S.; Guillot, R.; Lambert, F.; Policar, C. *Inorg. Chem.* **2014**, *53*, 6204–6223. (b) Jindabot, S.; Teerachanan, K.; Thongkam, P.; Kiatisevi, S.; Khamnaen, T.; Phiriyawirut, P.; Charoenchaidet, S.; Sooksimuang, T.; Kongsaree, P.; Sangtrirunugul, P. *J. Organomet. Chem.* **2014**, *750*, 35–40. (c) Stengel, I.; Mishra, A.; Pootrakulchote, N.; Moon, S.-J.; Zakeeruddin, S. M.; Gratzel, M.; Bauerle, P. *J. Mater. Chem.* **2011**, *21*, 3726–3734. (d) Gu, S.; Xu, H.; Zhang, N.; Chen, W. *Chem.-Asian J.* **2010**, *5*, 1677–1686.

(11) (a) Liu, S.; Lentz, D.; Tzschucke, C. C. *J. Org. Chem.* **2014**, *79*, 3249–3254. (b) Chattopadhyay, B.; Vera, C. I. R.; Chuprakov, S.; Gevorgyan, V. *Org. Lett.* **2010**, *12*, 2166–2169.

(12) Zhang, Q.; Wang, X.; Cheng, C.; Zhu, R.; Liu, N.; Hu, Y. *Org. Biomol. Chem.* **2012**, *10*, 2847–2854.

(13) Schweinfurth, D.; Pattacini, R.; Strobel, S.; Sarkar, B. *Dalton Trans.* **2009**, 9291–9297.

(14) (a) Hohloch, S.; Suntrup, L.; Sarkar, B. *Organometallics* **2013**, *32*, 7376–7385. (b) Zhang, C.; Shen, X.; Sakai, R.; Gottschaldt, M.; Schubert, U. S.; Hirohara, S.; Tanihara, M.; Yano, S.; Obata, M.; Xiao, N.; Satoh, T.; Kakuchi, T. *J. Polym. Sci., Part A Polym. Chem.* **2011**, *49*, 746–753. (c) Richardson, C.; Fitchett, C. M.; Keene, F. R.; Steel, P. J. *Dalton Trans.* **2008**, 2534–2537.

(15) (a) Connell, T. U.; Hayne, D. J.; Ackermann, U.; Tochon-Danguy, H. J.; White, J. M.; Donnelly, P. S. *J. Labelled Compd. Radiopharm.* **2014**, *57*, 262–269. (b) Clede, S.; Lambert, F.; Sandt, C.; Kascakova, S.; Unger, M.; Harte, E.; Plamont, M.-A.; Saint-Fort, R.; Deniset-Besseau, A.; Gueroui, Z.; Hirschmugl, C.; Lecomte, S.; Dazzi, A.; Vessieres, A.; Policar, C. *Analyst* **2013**, *138*, 5627–5638. (c) Seridi, A.; Wolff, M.; Boulay, A.; Saffon, N.; Coulais, Y.; Picard, C.; Machura, B.; Benoist, E. *Inorg. Chem. Commun.* **2011**, *14*, 238–242. (d) Boulay, A.; Seridi, A.; Zedde, C.; Ladeira, S.; Picard, C.; Maron, L.; Benoist, E. *Eur. J. Inorg. Chem.* **2010**, 5058–5062. (e) Obata, M.; Kitamura, A.; Mori, A.; Kameyama, C.; Czaplowska, J. A.; Tanaka, R.; Kinoshita, I.; Kusumoto, T.; Hashimoto, H.; Harada, M.; Mikata, Y.; Funabiki, T.; Yano, S. *Dalton Trans.* **2008**, 3292–3300.

(16) Farrugia, L. J. *J. Appl. Crystallogr.* **1997**, *30*, 565.

(17) (a) Mindt, T. L.; Struthers, H.; Brans, L.; Anguelov, T.; Schweinsberg, C.; Maes, V.; Tourwe, D.; Schibli, R. *J. Am. Chem. Soc.* **2006**, *128*, 15096–15097. (b) Bastero, A.; Font, D.; Pericàs, M. A. *J. Org. Chem.* **2007**, *72*, 2460–2468.

(18) (a) Huynh and co-workers have shown that benzimidazol-2-ylidene-dibromopalladium(II) complexes can be used to probe the σ -donor strength of the ligands *trans* to the benzimidazol-2-ylidene. They have found that there is a direct relationship between the σ -donor strength of the *trans* monodentate ligand and the chemical shift of the benzimidazole carbene carbon in the ^{13}C NMR spectra of the dibromopalladium(II) complexes. Very recently they have extended that system to include bidentate ligands, see the following: (b) Guo, S.; Sivaram, H.; Yuan, D.; Huynh, H. V. *Organometallics* **2013**, *32*, 3685–3696. (c) Huynh, H. V.; Han, Y.; Jothibasur, R.; Yang, J. A. *Organometallics* **2009**, *28*, 5395–5404. (d) Teng, Q.; Huynh, H. V. *Inorg. Chem.* **2014**, *53*, 10964–10973. (e) Yuan, D.; Huynh, H. V. *Organometallics* **2012**, *31*, 405–412.

(19) Lo, W. K. C.; Cavigliasso, G.; Stranger, R.; Crowley, J. D.; Blackman, A. G. *Inorg. Chem.* **2014**, *53*, 3595–3605.

(20) (a) Welby, C. E.; Armitage, G. K.; Bartley, H.; Wilkinson, A.; Sinopoli, A.; Uppal, B. S.; Rice, C. R.; Elliott, P. I. P. *Chem.-Eur. J.* **2014**, *20*, 8467–8476. (b) Welby, C. E.; Armitage, G. K.; Bartley, H.; Sinopoli, A.; Uppal, B. S.; Elliott, P. I. P. *Photochem. Photobiol. Sci.* **2014**, *13*, 735–738. (c) Welby, C. E.; Rice, C. R.; Elliott, P. I. P. *Angew. Chem., Int. Ed.* **2013**, *52*, 10826–10829. (d) Wachter, E.; Howerton, B. S.; Hall, E. C.; Parkin, S.; Glazer, E. C. *Chem. Commun.* **2014**, *50*, 311–313. (e) Glazer, E. C. *Isr. J. Chem.* **2013**, *53*, 391–400. (f) Wachter, E.; Heidary, D. K.; Howerton, B. S.; Parkin, S.; Glazer, E. C. *Chem. Commun.* **2012**, *48*, 9649–9651. (g) Howerton, B. S.; Heidary, D. K.; Glazer, E. C. *J. Am. Chem. Soc.* **2012**, *134*, 8324–8327.

(21) Adamo, C.; Barone, V. *J. Chem. Phys.* **1999**, *110*, 6158–6170.

- (22) Adams, C. J.; Fey, N.; Parfitt, M.; Pope, S. J. A.; Weinstein, J. A. *Dalton Trans.* **2007**, 4446–4456.
- (23) Cummings, S. D.; Eisenberg, R. J. *Am. Chem. Soc.* **1996**, *118*, 1949–1960.
- (24) Stein, P.; Miskowski, V.; Woodruff, W. H.; Griffin, J. P.; Werner, K. G.; Gaber, B. P.; Spiro, T. G. *J. Chem. Phys.* **1976**, *64*, 2159–2167.
- (25) Adams, C. J.; Fey, N.; Weinstein, J. A. *Inorg. Chem.* **2006**, *45*, 6105–6107.
- (26) O'Boyle, N. M.; Tenderholt, A. L.; Langner, K. M. *J. Comput. Chem.* **2008**, *29*, 839–845.
- (27) Schmid, E. D.; Brosa, B. *J. Chem. Phys.* **1972**, *56*, 6267–6268.
- (28) Wrighton, M.; Morse, D. L. *J. Am. Chem. Soc.* **1974**, *96*, 998–1003.
- (29) Caspar, J. V.; Meyer, T. J. *J. Phys. Chem. A* **1983**, *87*, 952–957.
- (30) Welby, C. E.; Grkinic, S.; Zahid, A.; Uppal, B. S.; Gibson, E. A.; Rice, C. R.; Elliott, P. I. P. *Dalton Trans.* **2012**, *41*, 7637–7646.
- (31) Gorelsky, S. I.; Dodsworth, E. S.; Lever, A. B. P.; Vlcek, A. A. *Coord. Chem. Rev.* **1998**, *174*, 469–494.
- (32) Bradley, P. G.; Kress, N.; Hornberger, B. A.; Dallinger, R. F.; Woodruff, W. H. *J. Am. Chem. Soc.* **1981**, *103*, 7441–7446.
- (33) Werrett, M. V.; Muzzioli, S.; Wright, P. J.; Palazzi, A.; Raiteri, P.; Zacchini, S.; Massi, M.; Stagni, S. *Inorg. Chem.* **2014**, *53*, 229–243.
- (34) Borg, O. A.; Godinho, S. S. M. C.; Lundqvist, M. J.; Lunell, S.; Persson, P. J. *J. Phys. Chem. A* **2008**, *112*, 4470–4476.
- (35) Osterman, T.; Abrahamsson, M.; Becker, H.-C.; Hammarström, L.; Persson, P. J. *J. Phys. Chem. A* **2012**, *116*, 1041–50.
- (36) (a) Krikorian, M.; Liu, S.; Swager, T. M. *J. Am. Chem. Soc.* **2014**, *136*, 2952–2955. (b) Li, Y.; Zhao, L.; Tam, A. Y.-Y.; Wong, K. M.-C.; Wu, L.; Yam, V. W.-W. *Chem.–Eur. J.* **2013**, *19*, 14496–14505. (c) Stengel, I.; Strassert, C. A.; Plummer, E. A.; Chien, C.-H.; De Cola, L.; Bäuerle, P. *Eur. J. Inorg. Chem.* **2012**, *2012*, 1795–1809.
- (37) Romeo, R.; Scolaro, L. M. *Inorg. Synth.* **1998**, *32*, 153–158.
- (38) Tong, A. Y. C.; Braund, R.; Tan, E. W.; Tremblay, L. A.; Stringer, T.; Trought, K.; Peake, B. M. *Environ. Chem.* **2011**, *8*, 182–189.
- (39) *CrysAlisPRO*; Oxford Diffraction /Agilent Technologies UK Ltd: Yarnton, England, 2012.
- (40) Altomare, A.; Burla, M. C.; Camalli, M.; Cascarano, G. L.; Giacovazzo, C.; Guagliardi, A.; Moliterni, A. G. G.; Polidori, G.; Spagna, R. *J. Appl. Crystallogr.* **1999**, *32*, 115–119.
- (41) Sheldrick, G. M. *Acta Crystallogr., Sect. A: Found. Crystallogr.* **2008**, *A64*, 112–122.
- (42) Farrugia, L. J. *J. Appl. Crystallogr.* **1999**, *32*, 837–838.
- (43) Nakamaru, K. *Bull. Chem. Soc. Jpn.* **1982**, *55*, 2697–2705.
- (44) Horvath, R.; Lombard, J.; Lepretre, J. C.; Collomb, M. N.; Deronzier, A.; Chauvin, J.; Gordon, K. C. *Dalton Trans.* **2013**, *42*, 16527–16537.
- (45) Frisch, M. J.; Trucks, G. W.; Schlegel, H. B.; Scuseria, G. E.; Robb, M. A.; Cheeseman, J. R.; Scalmani, G.; Barone, V.; Mennucci, B.; Petersson, G. A.; Nakatsuji, H.; Caricato, M.; Li, X.; Hratchian, H. P.; Izmaylov, A. F.; Bloino, J.; Zheng, G.; Sonnenberg, J. L.; Hada, M.; Ehara, M.; Toyota, K.; Fukuda, R.; Hasegawa, J.; Ishida, M.; Nakajima, T.; Honda, Y.; Kitao, O.; Nakai, H.; Vreven, T.; Montgomery, J. A., Jr.; Peralta, J. E.; Ogliaro, F.; Bearpark, M.; Heyd, J. J.; Brothers, E.; Kudin, K. N.; Staroverov, V. N.; Kobayashi, R.; Normand, J.; Raghavachari, K.; Rendell, A.; Burant, J. C.; Iyengar, S. S.; Tomasi, J.; Cossi, M.; Rega, N.; Millam, J. M.; Klene, M.; Knox, J. E.; Cross, J. B.; Bakken, V.; Adamo, C.; Jaramillo, J.; Gomperts, R.; Stratmann, R. E.; Yazyev, O.; Austin, A. J.; Cammi, R.; Pomelli, C.; Ochterski, J. W.; Martin, R. L.; Morokuma, K.; Zakrzewski, V. G.; Voth, G. A.; Salvador, P.; Dannenberg, J. J.; Dapprich, S.; Daniels, A. D.; Farkas, Ö.; Foresman, J. B.; Ortiz, J. V.; Cioslowski, J.; Fox, D. J. *Gaussian 09*, Revision A.02, Gaussian, Inc., Wallingford, CT, 2009.
- (46) Hay, P. J. W.; Willard, R. J. *J. Chem. Phys.* **1985**, *82*, 270–283.
- (47) Becke, A. D. *J. Chem. Phys.* **1993**, *98*, 5648–5652.
- (48) Stoyanov, S. S.; Yancheva, D. Y.; Stamboliyska, B. A. *Comp. Theor. Chem.* **2014**, *1046*, 57–63.